UNIVERSITY OF TROMSØ UIT

FACULTY OF SCIENCE AND TECHNOLOGY
DEPARTMENT OF PHYSICS AND TECHNOLOGY

Complexity in plasma and geospace systems

Tatjana Živković

A dissertation for the degree of
Philosophiae Doctor

May 2011

Summary

The subject of this thesis is self-organization, chaos and stochastic dynamics in laboratory plasmas, the magnetosphere, and in the Earth's climate system. For each of these systems we pose the question whether the global dynamics can be described by a set of a few variables governed by the same small number of deterministic equations. This problem is not trivial, because low-dimensional deterministic systems may exhibit chaotic dynamics where the solutions are sensitive to the initial conditions, and in most respects are indistinguishable from stochastic, noise-like dynamics.

A number of data analysis methods for time series are employed and adapted to the problems at hand. Among these methods are time-delay phase space reconstruction, correlation-dimension estimation of strange attractors, recurrence plots, empirical mode decomposition, wavelet decomposition, estimation of predictability and long-range memory, estimation of low-dimensional determinism of the dynamics, and principal value decomposition.

The analysis is complemented by numerical simulations of simple dynamic-stochastic model systems. Some of these have solutions with known properties, some low-dimensional and chaotic, and some are realizations of well-known stochastic processes. These are used to benchmark the analysis methods. Other models are designed to provide solutions with statistical properties very similar to those of the observational signals, and hence can be considered as minimal models for the phenomenon at hand.

The thesis consists of an introductory part and four journal papers. The former briefly reviews the basics of low-dimensional dynamical systems and the reconstruction of the phase-space attractor from experimental time series, long-memory stochastic processes, and critical phenomena with emphasis on self-organized critical dynamics. We also review the data analysis methods employed in this work, and finally we give an introduction to, and some examples from, the particular plasma laboratory and geospace systems which are studied in more detail in the papers. This part ends with a section where some of the analysis methods are employed to climate data. This section has been included because climate dynamics appears to be a promising field for application of these concepts and methods, although this author has not published or submittet journal papers on this application yet.

Paper I and Paper II deal with the detection of low-dimensional chaotic dynamics on time scales longer than those of the turbulent plasma dynamics in the laboratory Helimak configuration, and estimation of the largest Lyapunov exponent and the fractal dimension of the phase-space attractor. These estimates give us the degree of unpredictability and indicate how many equations we need to describe the chaotic dynamics.

In Paper III and Paper IV we estimate the degree of predictability and the organization of a deterministic component in the global magnetosphere during magnetic storms and substorms, respectively. These are accompanied by simultaneous estimations of solar wind parameters which are known to influence magnetospheric dynamics. From these results one may draw conclusions about the causal relationship between perturbations in the solar wind and in the magnetosphere, and infer that the organization of the magnetosphere during these events are internal processes and not imposed by an organization of the solar wind.

Acknowledgments

I would like to thank University of Tromsø and Department of physics and technology for giving me the opportunity to study an interesting and important subject.

My deepest thanks go to my great supervisor, prof. Kristoffer Rypdal. Criticism that I got from you have learnt me to be more sceptical about promising but sometimes premature results, to be more patient, more logical and more modest.

Your analytical and calm mind have not let me forget physics and sink in eternal computer programming. It was very inspiring having a supervisor, who is a real physicist and philosopher in heart from dawn to dusk, from pub to office, and always eager to fall into deep discussions.

My thanks go to Lene for sharing office with me, and making my stay in San Francisco funny and memorable.

To Hanne and Magnar for making my social life richer.

To John-Are and Adrian for being my energy and light, and keeping me down to Earth.

Til Anna som har hjulpet oss mye og som suverent har det største hjertet som en svigermor kan ha.

Mami i tati zahvaljujem zato što ste odustali od želje da i ja budem lekar i zato što se nikada niste protivili mojim snovima.

Tanja

Contents

Chapter 1

Introduction

1.1 Motivation

In the 1960s the theoretical meteorologist Edward Lorenz introduced a reduced set of nonlinear ordinary differential equations describing thermal convection in a fluid. By exploring different parameter regimes of these equations, he discovered that their solutions are very sensitive to the initial conditions. Unlike what was normally assumed, two solutions with almost the same initial conditions can diverge exponentially from each other as time progresses. After this discovery, the term *temporal chaos* was coined. Even more surprising, Lorenz was able to demonstrate that chaos can be produced from as few as three ordinary differential equations, and hence that the solutions of very simple, low-dimensional systems can be impossible to predict, even though existence and uniqueness of these solutions can be mathematically proven. This fact had been known to a handful of mathematicians, and proven by Henri Poncaré, but not recognized widely by the scientific community until the invention of digital computers made it clear to everybody who cares to know that low-dimensional chaos is real and ubiquitous.

Before Lorenz nobody would question that detailed prediction may be impossible in nonlinear systems of many degrees of freedom. After all, this unpredictability is the basis for the development of field of statistical physics. But the discovery of chaos in Lorenz' equations raised an important question: what is the difference between stochastic systems and low-dimensional, chaotic systems, since the outcome of both is impossible to predict on longer time scales? The answer to this question is not as simple in practice, since the microscopic description of most physical systems, including Lorenz' convecting fluids, involves an enormous number of degrees of freedom. Lorenz' derivation of his equations was a standard example of physical modeling where the high-dimensional microsopic description is reduced to a low-dimensional one through a critical sequence of approximations. The final justification of this reduction is that the reduced equations exhibit parameter regimes where the solutions are regular, periodic motion which can be observed in experiments. It is not difficult to conclude that such regular motion is low-dimensional. The difficulty arises when Nature presents us with dynamics that appear random and unpredictable. Is it high-dimensional, or is it low-dimensional and chaotic? The distinction is important, because in the former case the description must be statistical (stochastic). In the latter we may hope to describe the system by a small number of equations that can easily be

explored on a laptop. This problem is the main subject of this thesis.

The first part of my thesis is focused on detection of low-dimensional chaos in laboratory plasma. Here I apply several methods to discern the existence of low-dimensional chaos and then the dynamics revealed are interpreted according to known physics of the system under study. The plasma experiments are set up with the intention to study particular physics, and hence these systems are to some extent controlled. The chaos discovered occurs on slow time scales where the plasma interaction with the external circuit is important, and hence it can be influenced by the experimenter. Control theory is an example of an area where the understanding of chaotic dynamics is of immense practical importance.

The second part of my thesis is concerned with systems that are beyond human control: the magnetosphere and the climate. Each of these systems is highly dimensional, and their spatial structure is unpredictable over long distances, just like the temporal behavior. These systems confront us with *spatiotemporal chaos*, and complex-system approaches comes into focus. The theory of complexity is less developed than the theory of chaotic systems and concepts like turbulence, phase transitions, and self-organized criticality are unavoidable. Again the central issue in my work is to distinguish stochastic from low-dimensional dynamics, but now we do not only deal with the problem of detection of low-dimensional dynamics, but also the process of self-organization that produces such dynamics spontaneously or as a result of changes in external forcing. The coexistence of stochastic and low-dimensional dynamics is also an issue, and simple dynamic-stochastic models that encapsulate both are discussed.

1.2 Structure of thesis

Chapter 2 gives an introduction to some of the complex-system concepts and approaches employed in this thesis: chaos, stochastic processes, phase transitions and self-organized criticality. Chapter 3 reviews the methods employed in the data analysis. Chapter 4 shows results from plasma laboratory experiments, solar wind-magnetosphere interaction, and Earth's climate. This chapter concludes with a collection of four published and submitted research articles on these subjects.

1.3 Publication summary

1.3.1 Articles

Paper 1: Živković, T., and K. Rypdal, **Evidence of low dimensional chaos in magnetized plasma turbulence**, *Eur. Phys. J. Special Topics* **164**, 157, doi: 10.1140/epjst/e2008-00841-5, 2008

Abstract: We analyze probe data obtained from a toroidal magnetized plasma configuration suitable for studies of low-frequency gradient-driven instabilities. These instabilities give rise to field-aligned convection rolls analogous to Rayleigh-Benard cells in neutral fluids, and may theoretically develop similar routes to chaos. When using mean-field dimension analysis, we observe low dimensionality, but this could originate from either low-

dimensional chaos, periodicity or quasi-periodicity. Therefore, we apply recurrence plot analysis as well as estimation of the largest Lyapunov exponent. These analyses provide evidence of low-dimensional chaos, in agreement with theoretical predictions. Our results can be applied to other magnetized plasma configurations, where gradient-driven instabilities dominate the dynamics of the system.

Paper 2: Živković, T., and K. Rypdal, **Experimental evidence of low dimensional chaotic convection dynamics in a toroidal magnetized plasma**, *Phys. Rev. E* **77**, doi: 10.1103/PhysRevE.77.037401, 2008.

Abstract: In a toroidal plasma confined by a purely toroidal magnetic field with a weak vertical field superimposed a system of convection cells are generated spontaneously, interacting with a background electron density gradient. The dynamics of this interaction is low-dimensional, chaotic, and consistent with solutions of the Lorenz equations in the diffusionless limit.

Paper 3: Živković, T., and K. Rypdal, **Low-dimensionality and predictability of solar wind and global magnetosphere during magnetic storms**, submitted to *Journal of Geophysical Research.*

Abstract: The storm indices D_{st} and SYM-H and the solar wind velocity v and interplanetary magnetic field B_z show no signatures of low-dimensional dynamics in quiet periods, but tests for determinism in the time series indicate that SYM-H exhibits a significant low-dimensional component during storm time, suggesting that self-organization takes place during magnetic storms. Even though our analysis yields no discernible change in determinism during magnetic storms for the solar wind parameters, there are significant enhancement of the predictability and exponents measuring persistence. Thus, magnetic storms are typically preceded by an increase in the persistence of the solar wind dynamics, and this increase is reflected in the magnetospheric response to the solar wind.

Paper 4: Živković, T., and K. Rypdal, **Organization of the magnetosphere during substorms**, submitted to *Journal of Geophysical Research.*

Abstract: The change in degree of organization of the magnetosphere during substorms is investigated by analyzing various geomagnetic indices, as well as interplanetary magnetic field z-component and solar wind flow speed. We conclude that the magnetosphere self-organizes globally during substorms, but neither the magnetosphere nor the solar wind become more predictable in the course of a substorm. This conclusion is based on analysis of five hundred substorms in the period from 2000 to 2002. A minimal dynamic-stochastic model of the driven magnetosphere that reproduces many statistical features of substorm indices is discussed.

1.3.2 Other publications and presentations

As first author:

1. Živković, T., and K. Rypdal, On the dynamics of the magnetosphere during geomagnetic storms and substorms. Poster at *American Geophysical Union Fall meeting*, San Francisco, December 2010.

2. Živković, T., and K. Rypdal, Recurrence plot techniques applied to solar wind- magnetosphere interaction. Oral presentation at *The Birkeland Workshop*, Tromsø, May 2010.

3. Živković, T., and K. Rypdal, Dynamics of the Auroral Electrojet Index Time Series. Poster at *American Geophysical Union Fall Meeting*, San Francisco, USA, December 2008.

4. Živković, T., L. Østvand, K. Rypdal, On the connection between the multifractality and the predictability from the auroral index time series. Poster presentation at *24rd Summer School and International Symposium on the Physics of Ionized Gases*, Novi Sad, Serbia, August 2008. Published in *Publications of the Astronomical Observatory of Belgrade*, vol. 84, pp. 511-514, 2008.

5. Živković, T., and K. Rypdal, Low-dimensional dynamics in magnetized plasma turbulence. Poster presentation at *Recurrence plot workshop*, Sienna, Italy, September 2007.

6. Živković, T., and K. Rypdal, Routes to chaos in Helimak device. Oral presentation at *Biannual meeting of the Norwegian Physical Society*, Tromsø, August, 2007.

7. Živković, T., and K. Rypdal, Low dimensional chaos in experimental data from Helimak device. Poster presentation at *Chaos, Complexity and Transport: Theory and Application*, Marseille, France, June, 2007.

8. Živković, T., and K. Rypdal, Langevin approach to SOC. Oral presentation at *Workshop on Complexity in Plasma and Geospace systems* in Geilo, Norway, March, 2007.

9. Živković, T., and K. Rypdal, Indication of low dimensional dynamics in geomagnetic time series. Oral presentation at *Annual meeting of the Norwegian Geophysical Society*, Geilo, Norway, September, 2006.

As coauthor:

1. Rypdal, K., M. Rypdal, B. Kozelov, T. Živković, L. Østvand, Stochastic modeling of fluctuations in large-scale properties of the Solar wind or the magnetosphere-ionosphere system. Poster at *American Geophysical Union Fall meeting*, San Francisco, Desember 2008.

2. Rypdal, K.,and T. Živković, Burst statistics of fluctuations in a simple magnetized torus configuration. Oral presentation at *EFTSOMP workshop*, Heraklion, Greece, June 2008.

3. Rypdal, K., M. Rypdal, B. Kozelov, S. Servidio, T. Živković, Complexity in astro- and geospace systems: the turbulence versus SOC controversy, *AIP Conference Proceedings*, Volume 932, pp. 203-208, 2007.

Chapter 2

Complex systems

This thesis deals with analysis and modeling of physical systems: laboratory plasmas, Earth's magnetosphere, and climate, which have little in common when it comes to the microscopic physics. Nevertheless, the methods used for analysis are essentially the same for all systems, and the conceptual and stochastic models employed have a lot in common. This is possible due to the choice of a scientific approach, the complex-system approach, which is focused on *structure* rather than *detail* [1]. This choice does not necessarily imply subscription to a belief that this approach is "better" or more "truthful" than the reductionist approach based on first physical principles. However, the trend in scientific communities is towards increasing recognition that the two approaches complement each other and that complex-system approaches are becoming an integral part of modern science. This chapter will give a brief review of some fundamental themes and concepts that are central in complex-system science and central to the results reported in the journal articles presented in chapter 4.

2.1 Chaos

The concept of deterministic chaos has its root in the mathematics of dynamical systems [2]. The mathematical structure is often explored via discrete dynamical systems (maps), but in physical applications continuous formulations in the form of autonomous systems of ordinary differential equations are often more relevant. Such a system has the general form:

$$\frac{d\mathbf{x}}{dt} = \mathbf{f}(\mathbf{x}), \tag{2.1}$$

where $\mathbf{x}(t)$ is an n-dimensional vector representing the physical state of the system. The term *autonomous* means that the flow field $\mathbf{f}(\mathbf{x})$ does not depend explicitly on time. This implies that the entire trajectory $\mathbf{x}(t)$ for $-\infty < t < \infty$ is uniquely given if the position $\mathbf{x}$ at a given time (the initial condition) is known. This is what we mean when we state that dynamical systems are deterministic. The basic microscopic laws of classical physics can be formulated as dynamical systems, and hence they are deterministic. The n-dimensional space hosting the state vector $\mathbf{x}$ is called the *phase space*, and the evolution of the system constitutes a trajectory in this space. The family of all these trajectories is called a *flow*,

and the set of points enclosed by a closed surface in phase space that moves with the flow can be thought of as a volume of the *phase-space fluid*.

If a dynamical system is in equilibrium $f(\mathbf{x}_p) = 0$, or $\mathbf{x}_p$ is a fixed point of the system. In linear systems, there is exactly one $\mathbf{x}_p$, while nonlinear systems can have none, one, or many fixed points. Further, $\mathbf{x}_p$ can be either stable or unstable, depending whether nearby initial conditions are attracted or repelled from it. Unstable fixed points for which some trajectories in phase space are attracted to x_p, while others are repelled are called a saddle points. These are often involved in producing the conditions for chaos, since they may provide stretching and folding of trajectories in the phase space. Saddle points are also the most common type of equilibrium in high-dimensional systems.

Only dissipative systems have attractors in phase space. A physical system is called *dissipative* if its energy is dissipated into a heat. This action contracts the volume of fluid elements in the phase-space fluid as time progresses. Strange attractors are fractal objects whose dimension is not an integer number. They are transitive (the dynamics of any point on the attractor will take us arbitrarily close to any other point on the attractor); they are structurally stable (any addition of small terms in the equations or a change in parameters should not change the attractor); they are usually sensitive to the initial conditions, meaning that two nearby initial conditions should separate exponentially on average. This is the most striking property of low-dimensional chaotic systems, since it implies that prediction is impossible on time scale longer than the characteristic time scale of this exponential growth. The exponential growth rate is determined by the largest Lyapunov exponent of the system, and is a quantity that is possible to compute from time-series of quantities that measure the evolution of the state of the system.

In figure 2.1 we show an example of the Lorenz attractor, which emanates from the dynamical system:

$$\begin{aligned} dx/dt &= a(y-x) \\ dy/dt &= -xz + cx - y \\ dz/dt &= xy - bz, \end{aligned} \tag{2.2}$$

where $a = 10$, $b = 8/3$ and $c = 28$. Here, the attractor resembles a butterfly. Chaos is produced by random sweeping of the trajectory from one "wing" of the butterfly to another. In a discrete systems (maps) chaos can occur in one and two dimensions, while for continuous flows chaos is possible only in three dimensions or higher, since trajectories in the phase space are not allowed to cross each other [3]. With two-dimensional, continuous flows, trajectories can only approach a fixed point or limit cycle, or go to infinity.

Hamiltonian chaos can take place in physical systems where energy is conserved. This conservation implies that phase-space volumes are preserved as time progresses. The mechanism of Hamiltonian chaos is overlap between regions of periodic motion in phase space (resonance overlap). These systems do not have phase-space attractors and different initial conditions can give rise to different dynamics (chaos, periodic motion, etc.).

In low-dimensional dynamical systems transient behavior is followed by asymptotic motion converging to the attractor, covering it densely as time evolves. We will be interested in determining geometrical properties of the attractor. Is it a fixed point, a limit cycle, quasi-periodic motion, or a strange attractor. And in the latter case, what is the fractal dimension of the attractor?

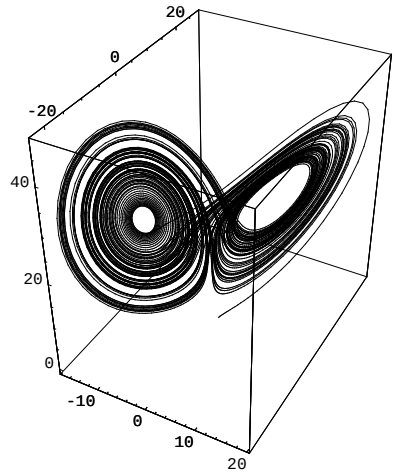

Figure 2.1: Lorenz attractor

If the dynamics is very complex or if the system is high-dimensional, statistical and thermodynamical descriptions like *invariant measures* are more useful than exploration of geometrical structure of attractors. One approach to understanding turbulence is by modelling as high-dimensional dynamical systems [4]. However, distinguishing high-dimensional, deterministic and chaotic systems from stochastic systems is notoriously difficult. In principle one could study how sample paths with almost identical initial conditions diverge with time. It is known that while chaotic paths diverge exponentialy, stochatic paths diverge like a power-law. An even more important difference is that while two chaotic paths starting out at nearby points in phase space will move in the same direction for some tome before they separate, stochastic paths will move in arbitrary and different directions. The latter property will be used in Papers III and IV in this thesis to distinguish low-dimensional, chaotic motion from stochastic. Unfortunately the method does not work for high-dimensional systems because we are not able to reconstruct from time-series data a state vector that represents the full state of the system in n-dimensional phase space. The best we can hope for is to reconstruct a projection of this vector onto a low-dimensional space, and then two reconstructed vectors which are close in the reconstructed space may represent two states that are widely separated in the full phase space. The implication is that evolution that appears stochastic from analysis of reconstructed state vectors may well be a result of high-dimensional deterministic dynamics.

This brings us over to the subject of how to reconstruct a phase space from the method of time-delay embedding.

2.2 Embedding

The concept of phase space was first introduced in the field of theoretical and statistical mechanics, where generalized coordinates and momenta $(q_i, p_i), i = 1, \ldots, N$ are introduced and N is the number of degrees of freedom. In this case the phase space has dimension $n = 2N$. If the output of an experiment or the observation of a natural system has the

form of a time series $s(t)$ we may attempt to reconstruct a phase space of lower dimension m in which the attractor of the dynamics is topologically (continuously and one-to-one) embedded. The most common reconstruction method is the time-delay embedding [5], but also differential embedding, Hilbert transform embeddings as well as Singular Value Decomposition embedding [6]. In all approaches, it is assumed that embedding creates a diffeomorphism between the underlying, experimental attractor and embedded, or reconstructed, chaotic attractor. If the underlying dynamic, which we can not measure directly, in its original phase space can be explained by a trajectory $x(t) = f^t(x(0))$, and if there is a measurement function h, such that $s(t) = h(x(t))$, then the reconstruction according to the time-delay embedding is obtained as:

$$F(x) = [h(x), h(f^\tau(x)), h(f^{2\tau}(x)), \ldots, h(f^{(m-1)\tau}(x))] \tag{2.3}$$

where τ is a time-delay, chosen to be bigger than the sampling rate and smaller than the decorrelation time of the time series $s(t)$. However, this reconstruction is valid only for autonomous systems. If there is a driver in the system, not only output time series $s(t)$ is enough, but also input time series $I(t)$ is needed [7]. The reconstruction is then as follows:

$$\begin{aligned}(I_t^T, s_t^T) = \\ (I_t, I_{t+\tau}, ..., I_{t+(m_i-1)\tau}, s_t, s_{t+\tau}, ...s_{t+(m_o-1)\tau}),\end{aligned} \tag{2.4}$$

which found application in driven-dynamical systems as we demonstrate on the example of laboratory plasma in Paper I. The estimate for the embedding dimension m was given in [8], and represented the number of eigenvalues over the noise level, if obtained from the singular system analysis. Another estimate for m can be obtained from the following contemplation: If the attractor is properly reconstructed, its dimension is not dependent of further increase of m. On the other hand, for stochastic systems, the phase space attractor has infinite dimension, and with the increase of the embedding dimension, distances between the points and the dimension of the attractor continue to increase. The reason for this behavior is that for lower m, the attractor of the dynamics projects to the lower dimension and points that are far apart might appear closer. However, when the embedding dimension is appropriate, all trajectories are "unfolded" and with a further increase of m, attractors dimension does not change.

A sufficient condition is $m \geq 2d + 1$ where d is the dimension of the attractor of the dynamics, since then trajectories should not intersect in the embedded space [9]. In order to compute d, a common method is to calculate correlation integral developed by Grassberger and Proccacia (1983) [10], which is given by the following formula:

$$C(r) = \frac{2}{N(N-1)} \sum_{i=1}^{N} \sum_{j=i+1}^{N} \Theta(r - \|x(i) - x(j)\|), \tag{2.5}$$

where $\Theta(a) = 1$ if $a \geq 0$ and $\Theta(a) = 0$ otherwise. Here r is radius of the ball in the phase space. If there is an attractor in phase space $C(r) \sim r^d$, and the correlation dimension can be defined as $D = \log(C(r))/\log(r)$. If the dynamics is periodic or quasi-periodic the correlation dimension D is equal to the topological dimension d of the attractor, while for a chaotic systems we have a strange attractor and then the fractal dimension D is usually

not an integer. It was shown by Osborne and Provenzale (1989) [11] that a time series with strong time correlations can also produce low correlation dimension, even if it is otherwise a linear, high-dimensional (stochastic) system. This will be discussed in more details in section 4.1.

In the case of experimental time series, different types of noise are present, which destroy the smoothness of the phase space attractor. In these computations, mean-field dimensional analysis is useful. This method is explained in detail in Paper I. The limitations of the time-delay embedding are that short or oversampled time series can produce artificially smaller correlation dimension. In addition, a presence of noise can distort trajectories and artificial intersection between trajectories can occur. Also, stochastic time series with time correlations (as mentioned) can produce low correlation dimension which is due to long memory in the signal rather than deterministic dynamics.

When the reduced phase space is reconstructed, we can measure the evolution of nearby trajectory segments by computation of Lyapunov exponents, which for a one-dimensional map $x_{n+1} = f(x_n)$ is defined as follows:

$$\lambda = \lim_{N\to\infty} \frac{1}{N} \sum_{i=0}^{N-1} \ln |f'(x_i)|, \tag{2.6}$$

For a continous flow in higher dimension n the definition is generalized, and there will be n Lyapunov exponents. But the equation above gives the idea and shows that the (largest) Lyapunov exponent is a measure of the average exponential rate of separation of two nearby initial conditions. If the system is periodic, it is enough to average over only one period once the orbit has reached the attractor. In a dissipative chaotic system, the sum of all Lyapunov exponents is negative implying the phase space contraction. Hamiltonian systems are time-reversible, and sum of Lyapunov exponents goes to zero. However, at least one of these Lyapunov exponents is positive if chaos present. Also, one of Lyapunov exponents has to be zero, which corresponds to the direction of the flow [12]. An example is Lorenz attractor which consists of three equations and hence, has three Lyapunov exponents: $\lambda \simeq 0.9065, 0, -14.5723$. If all Lyapunov exponent are zero the dynamics is continuous and predictable than randomly fluctuating. If the correlation dimension grows with the embedding dimension, negative Lyapunov exponents should not be obtained. White noise can only be reconstructed in an infinite-dimensional phase space and only then will its Lyapunov exponent be zero [13]. Since there is no algorithm for computing Lyapunov exponents which allow embedding dimension go to infinity, algorithms usually give positive Lyapunov exponents when applied to white noise. Too high embedding dimension in the computation of Lyapunov exponents may give incorrect results because noise, being infinite dimensional, may corrupt the data. All positive Lyapunov exponents give the estimate of the average rate at which predictability is lost.

2.3 Stochastic processes

A primary goal in this thesis is to devise methods to distinguish from data between deterministic and chaotic dynamics on one hand, and stochastic dynamics on the other. However, high-dimensional chaotic systems have many of the same statistical properties as time series

from stochastic processes. Therefore, many different tests have to be employed in order to disentangle stochastic and deterministic system properties from time-series data. By time series, we mean a sequence of numerical values x_i. Often we can think of the time series as a discrete sampling of a continuous stochastic process $\{x(t)\}$, such that $x_i = x(i\Delta t)$, where typically t is interpreted as the time variable.

For long, stationary time series it is meaningful to divide the data record into a number of subrecords of length T. Each subrecord is then Fourier transformed to yield $\tilde{x}(f)$, the power $\tilde{x}(f)^2$ is formed, and then averaged over the ensemble of subrecords to yield the spectral density function (SDF) $S(f) = \langle|\tilde{x}(f)|^2\rangle$. The frequency resolution of the discrete Fourier transform is $\Delta f = 1/T$ and the maximum (Nyquist) frequency is $f_N = 1/(2\Delta t)$. Let $\mathrm{var}\{\cdot\}$ denote the variance and $\sigma^2 = \mathrm{var}\{x_i\}$. Since the process $\{x_i\}$ is assumed to be stationary σ^2 and σ_i^2 do not depend on the index i. For such a process the autocorrelation function (ACF)

$$C(k\Delta t) = E\{x_i x_{i+k}\}/\sigma^2 \tag{2.7}$$

can also be given as the Fourier transform of $S(f)/\sigma^2$ in the interval $-T/2 < \tau < T/2$ with time resolution Δt. Here $E\{\cdot\}$ denotes the expectation value.

A standard method for studying the correlation structure on different time scales is to divide the time-series containing N data points into subrecords of lengths $m = 2n$ data points, where $n = 0, 1, 2, ..., M$, and $2M$ is much smaller than the total record length. For each value of n the value of the data points in each subrecord are averaged to produce new coarse grained time series. In practice the increasingly coarse grained time series are generated iteratively by generating the series corresponding to $n = 1$ from the original series ($n = 0$) by taking the mean of the first and second data point, the mean of third and the fourth data point, and so on until a series containing $N/2$ data points has been generated. Then a series ($n = 2$) containing $N/4$ points is constructed from performing the same operation on the $n = 1$ series, and so on up to $n = M$. If the original time-series is a realization of a stationary stochastic process x_i, where $i = 1, 2, ..., N$, and x_i are independent random variables, the variance σ_m^2 of the coarse grained time-series varies asymptotically as m^{-1} when $m \to \infty$. If the the random variables are not independent, the expression for σ_m^2 can be written

$$\sigma_m^2 = \mathrm{var}\{m^{-1}\sum_{k=0}^{m-1} x_{i+k}\} \approx [1 + 2\sum_{k=0}^{m-1} C(k\delta t)] \tag{2.8}$$

The asymptotic dependence $\sigma_m^2 \sim m^{-1}$ remains unchanged in the presence of correlations if the integral over the ACF is finite, i.e. if $\sum_{k=0}^{\infty} C(k\Delta t) < \infty$. However, if the integral diverges, as is the case if there exist real constants $a > 0$ and $0 < \alpha < 1$ such that $\lim_{\tau\to\infty} C(\tau)\alpha = a$ we rather find the asymptotic dependence $\sigma_m^2 \sim m^{-\alpha}$ as $m \to \infty$. This result can be written in the form

$$\lim_{\tau\to\infty} m^{1-H}\sigma_m = c, \tag{2.9}$$

where c is a constant and we have introduced the *Hurst exponent* $H = 1 - \alpha/2$. If a stationary time series satisfies condition (2.9) with $1/2 < H < 1$, it is said to exhibit *long range dependence* [14].

An equivalent definition of long range dependence in a stationary time series is that there exist real constants $b > 0$ and $0 < \beta < 1$ such that

$$\lim_{f \to 0} S(f) f^{\beta} = b. \tag{2.10}$$

Here, the exponents α, β, and H are related through

$$\alpha = 2 - 2H, \quad \beta = 2H - 1, \tag{2.11}$$

and hence $\alpha + \beta = 1$. While the Hurst exponent expresses increasing long-range dependence as H increases from $1/2$ to 1, for an important class of stochastic processes it also is called the selfsimilarity parameter [15]. A continuous stochastic process $y(t)$ is statistically selfsimilar if the rescaled process $\lambda^{-H} y(\lambda t)$ is equal *in distribution* to the original process $y(t)$ for any positive stretching factor λ. This means that for any sequence of time points $t_1, ..., t_k$ and any positive constant λ, the random variables $\lambda^{-H}(y(\lambda t_1), ..., y(\lambda t_k))$ have the same joint distribution function as $(y(t_1), ..., y(t_k))$. The process $y_i = y(i\Delta t)$ is selfsimilar in the continuous limit if the increment process $x_i = y_i - y_{i-1}$ is stationary and consists of independent random variables or exhibits long-range dependence.

The equivalence of the selfsimilarity parameter for the process y_i and the Hurst exponent for the increment process x_i defined by equation (2.9) is seen as follows: If x_i are stationary increments of a self-affine process y_i the sample mean can be written

$$\bar{x}_m = m^{-1}(y_m - y_0) \stackrel{d}{=} m^{-1} m^H (y_1 - y_0) = m^{H-1} x_1, \tag{2.12}$$

where $\stackrel{d}{=}$ denotes identity in distribution and H is the self-similarity parameter. From this we find that

$$\sigma_m^2 = \mathrm{var}\{\bar{x}_m\} = \sigma^2 m^{2H-2}, \tag{2.13}$$

which is equivalent to equation (2.9).

One tool for computing the Hurst exponent from a stationary time series $\{x_i\}$ is to construct the cumulative sum $y_i = \sum_{j=1}^{i} x_j$ and to compute the variogram

$$\gamma_m = \frac{1}{(N-m)} \sum_{i=1}^{N-m} (y_{i+m} - y_i)^2. \tag{2.14}$$

γ_m is an estimate of $\mathrm{var}\{m\bar{x}_m\}$, and hence if $\{y_i\}$ is selfsimilar with selfsimilarity parameter H we have from equation (2.13) that

$$\gamma_m \sim m^{2H}. \tag{2.15}$$

It is easy to show that if the stationary process $\{x(t)\}$ has a power-law SDF $S(f) \sim f^{-\beta}$, the integrated non-stationary process $\{y(t)\} = \{\int^t x(t')\, dt\}$ also has a power-law SDF with spectral index $\beta' = \beta + 2$. For instance, if $\{x(t)\}$ is a Gaussian white noise we have $\beta = 0$, and $H = (\beta + 1)/2 = 0.5$. However, the non-stationary process $\{y(t)\}$ has selfsimilarity exponent $H = 0.5$ and spectral index $\beta' = 2$, and is called a Brownian motion. For $0 < H < 1$ the stationary process $\{x(t)\}$ is called a fractional Gaussian noise (fGn) if it is

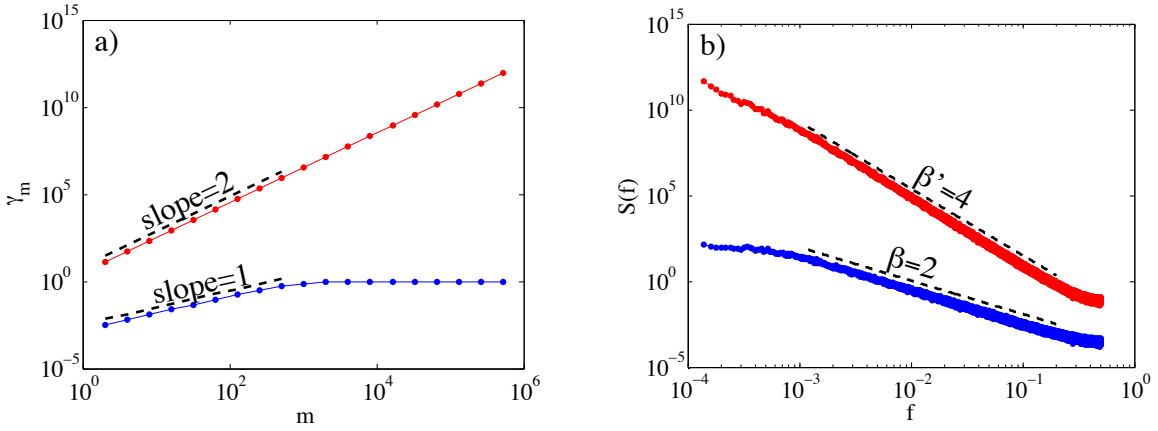

Figure 2.2: Variogram and power spectral density for Ornstein-Uhlenbeck process; blue is for original signal, red is for cumulative sum. a) Variograms. b) Power spectral densities.

Gaussian, and $\{y(t)\}$ is a fractional Brownian motion (fBm). If $\{w(t)\}$ is a white Gaussian noise the Langevin equation

$$\frac{dy}{dt} = -\nu y + \sqrt{D}\, w(t) \tag{2.16}$$

generates the so-called Ornstein-Uhlenbeck (O-U) process. Here ν is damping, and D is diffusion coefficient. The discrete version of this equation is a difference equation generating the AR(1) process. On time scales $\tau \ll \nu^{-1}$ the O-U process is non-stationary and identical to a Brownian motion, but on time scales $\tau \gg \nu^{-1}$ it becomes stationary and behaves like a white noise process. This is reflected in the SDF for the process, which by Fourier transforming equation is easily found to be a Lorentzian

$$S(f) \sim \frac{1}{(2\pi f)^2 + \nu^2}. \tag{2.17}$$

Above we have defined the Hurst exponent for stationary processes from the power-law behavior of the ACF $C(\tau)$ in the limit of $\tau \to \infty$ or of the SDF $S(f)$ in the limit $f \to 0$. We have also seen that it can be estimated from the power-law behaviour of the variogram γ_m in the limit $m \to \infty$ of the cumulative sum $y_i = \sum_{j=1}^{i} x_j$. However, for the O-U process we observed that power-law scaling properties may also exist in restricted regimes of time scales, and not only in the asymptotic limit of infinite time scales. The definition of H from the asymptotic properties of the autocorrelation function makes sense only for stationary processes for which $0 < H < 1$. In the literature, however, it is not uncommon to see Hurst exponents outside this range (as in Paper III). In those cases one should really consider this exponent as an extension of the definition of H based on its relation to the spectral index given by equation (2.11), i.e. $H \equiv (\beta + 1)/2$. With this definition, we would for instance have that the Hurst exponent for a Brownian motion ($\beta = 2$) would be $H = 1.5$, while the selfsimilarity exponent for this non-stationary process is $h = 0.5$. Thus, for motion we would have the relation

$$H = h + 1. \tag{2.18}$$

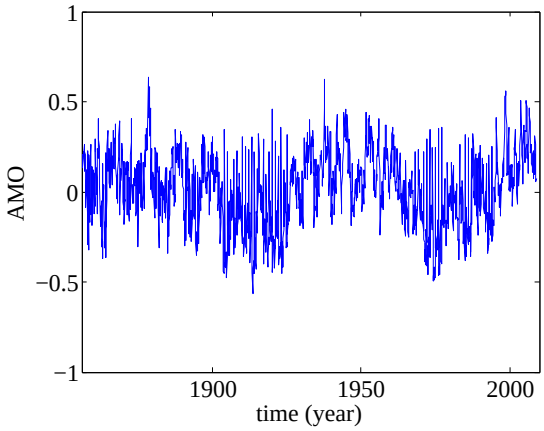

Figure 2.3: Atlantic Multidecadal Oscillation.

In figure 2.2 a) the red curve is the variogram of the cumulative sum of the O-U process in a log-log plot. On time scales $m\Delta t \ll \nu^{-1}$ the process is a Brownian motion and we should have $H = 1.5$. Since the scaling $\gamma_m \sim m^{2H}$ implies that $\log \gamma_m = 2H \log m + const$ the slope of the curve for $m\Delta t \ll \nu^{-1}$ should be 3. However, the slope in the figure is 2, demonstrating that the variogram does not work when applied to the cumulative sum of non-stationary processes (for which $H > 1$). However, for such processes the variogram can be applied to the process itself, as done in the blue curve in figure 2.2 a). In this case we find the self-similarity exponent h from the relation slope=$2h$. Since the slope for $m\Delta t \ll \nu^{-1}$ is 1 we find that $h = 0.5$ and hence that $H = h + 1 = 1.5$. On time scales $m\Delta t \gg \nu^{-1}$ the O-U process is a white noise. However, for noises (stationary processes) the variogram of the process itself is flat, and does not provide information about the Hurst exponent. To obtain information about the Hurst exponent in those cases where the variogram does not work, an alternative is to estimate the SDF and identify power-law regimes in the spectrum from log-log plots. This is done for the O-U process in figure 2.2 b) for the original signal and the cumulative sum. Since $H = 1.5$ in the short time-scale regime (large f) the slopes in the figure confirm the relations $\beta' = \beta + 2$ and $\beta = 2H - 1$. In the low-frequency regime the process is white noise and the slope of the blue curve should be 0, while on the red curve it should be 2. This is not perfect in this figure because the Fourier transform has been estimated on too short time windows.

The property that a signal is a non-stationary process (*a motion*) on short time scales, and stationary (a *noise*) on longer time scales is a property shared by a very large class of experimental and observational signals. The motion is not always Brownian, however, and the noise does not have to be white. The signals often exhibit long-range memory, and they are often non-Gaussian. Examples of such signals are discussed in all the journal articles included in this thesis.

As an example of a signal where it can be of interest to compute the Hurst exponent, we show in figure 2.3 the Atlantic Multidecadal Oscillation (AMO) index, which is spatially averaged sea surface temperature anomaly in the North Atlantic.

In figure 2.4 we show the variogram for the cumulative sum $y_i = \sum_{j=1}^{i} x_j$ of the AMO

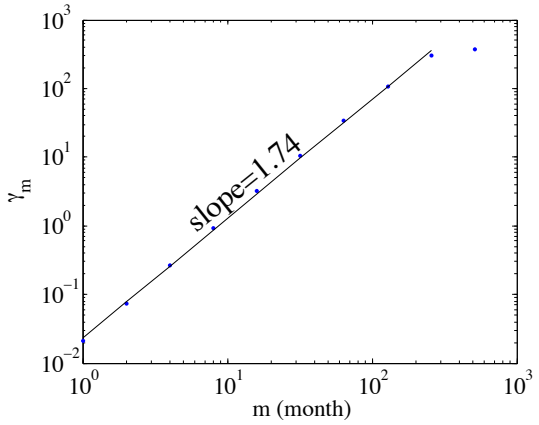

Figure 2.4: Variogram for cumulative sum of AMO.

signal. The slope is $2H = 1.74$, and hence $H = 0.87$ and the spectral index is $\beta = 2H - 1 = 0.74$. This indicates that the AMO signal is fractional Gaussian noise on the scales less than 300 months ($\sim$ 25 years), while on the longer scales it behaves as a white noise. This example, however, also illustrates one of the pitfalls of uncritical application of variogram and spectral analysis. Visual inspection of the AMO signal immediately reveals the existence of a slow oscillation with period of approximately 60 years, so the cumulative sum of the signal is obviously not completely self-similar. By removing this oscillatory trend (for instance by subtracting a low-pass filtered version of the signal) and the performing the variogram or spectral analysis one finds a somewhat lower Hurst exponent, but still there is a clear persistence ($H > 0.5$).

In contrast, variogram analysis for the x-component of the numerical solution of the Lorenz equations yields $H = 1$ on time scales $\tau \ll \lambda_1^{-1}$, where λ_1 is the largest Lyapunov exponent. This indicates that the solution is deterministic and predictable on this time scale. On time scales $\tau \gg \lambda_1^{-1}$, however, the variogram of the cumulative sum yields $H = 0.5$, and the SDF yields $\beta = 0$, demonstrating the lack of correlations and the white noise character of the chaotic signal on these time scales.

2.4 Critical phenomena

In thermodynamics, a phase transition represents the transformation of a system from one phase to another. By *phase* is meant a set of states of a macroscopic physical system which have relatively uniform chemical composition and physical properties such as density, index of refraction, etc. Some phase transitions either need supply of or release of energy during the process of transition and these are coined *first order phase transition*. During the energy transfer mixed-phase regimes are encountered, where some parts of the system have ended the transition and some have not. The most common example of the first order transitions are ice -to water- to vapor transition.

When there is no energy change between the phases, *second order phase transitions* take

place. These transitions are continuous and the ferromagnetic transition is one example. The phenomena associated with second order phase transitions are also called *critical phenomena*, since they can be characterized by parameters known as *critical exponents*. Close to criticality, these transitions exhibit power law behavior. For example, in some thermodynamic system, if all variables are kept constant except temperature, then close to the critical temperature T_c, heat capacity C of the system behaves as $C \sim |T_c - T|^{-\alpha}$, where α is the critical exponent. A remarkable fact about these transitions is that different systems can still have the same set of critical exponents. This phenomenon is known as *universality*. For example, the critical exponents at the liquid-gas critical point are independent of the chemical composition of the fluid [16].

A particular class of critical phenomena which has been proposed as a mechanism to explain the ubiquity of power-laws in Nature is the paradigm of self-organized criticality (SOC). This concept was first introduced by Per Bak et al. (1987) [17] who developed a discrete cellular automaton model, in order to illustrate how a sand pile responds to randomly added sand grains. In this case, grains of sand are dropped on the sand pile until its slope reaches some critical angle of repose. One might expect that additional sand drops in the critical state of slope would just slide down the slope. However, what really happens in an SOC system, is that an additional grain, when the critical state is approached, causes avalanches of various sizes with power-law distributed size and duration. On average, the number of added drops balances the number of drops that slide down the sand pile, but the actual number of grains fluctuates continuously. Experimental sand piles do not behave as SOC systems [18], so the term "sandpile model" should be understood as a class of cellular automata, not as a model for how real piles of sand behave.

SOC can be defined as a specific state of a slowly driven many-body (many grains) system characterized by an intermittent scale-free response to external perturbations, and marginal stability, implying the ability of the system to adjust to driving rate changes without losing its signatures of critical dynamics [19]. From the simple analogy with a sand pile, we can also conclude that the basic interactions in an SOC state are local, but long-range interactions develop due to the formation of a scale free distribution of avalanches near the critical state. Contrary to second order phase transitions near the critical point, SOC is shown to be robust and to arise spontaneously without tuning of system parameters, although it also can be argued that the limit of vanishing driving rate is also some sort of tuning [20]. Also, second-order phase transitions have at least one more class of critical exponents that relates the input parameters of the system (temperature) to its output (magnetization or density). The introduction of models that exibit self-organized criticality has been a major advance in extending concepts of chaos to higher order systems, i.e. by increasing number of degrees of freedom in the system, the transition from low dimensional chaos to self organized criticality can be studied [21]. In an SOC model, there is always a slow time-scale for the driver and a fast time-scale for the dissipation of the avalanches. For example, stress in the tectonic plates can be accumulated for years, and then relived in seconds in the form of earthquakes. SOC has become explanation for various systems, like earthquakes [22], plasma transport [23], stock prices [24], wars [25], etc.

Chapter 3

Methods

3.1 Recurrence plots

Recurrence plot (RP) analysis is one of the central tools employed throughout this PhD thesis. Their most obvious attractive feature is that direct visual interpretation is possible, and periodic, quasiperiodic/ chaotic, and noisy systems can be distinguished by eye. In RP different measures of complexity can be defined and some of them can be used as indicators of changes in the system's dynamics ([26], [27]). A particular advantage of RPs is that they can be applied to non-stationary and short time series as well as to systems with underlying nonlinear dynamics.

Recurrence is a fundamental characteristics of conservative and dissipative dynamical systems, reflecting that the phase-space orbit is dense on the attractor. This property, however, does not tell how long time it takes for a recurrence to occur, and this period can be very long for high-dimensional dynamical systems. RP is a plot of a matrix $R_{i,j}$ where in every matrix element two states at discrete time i and time j are compared. If these states are similar (i.e. their separation in phase space is small) $R_{i,j} = 1$, otherwise $R_{i,j} = 0$. Matrix elements for which $R_{i,j} = 1$ are plotted as black dots, while elements for which $R_{i,j} = 0$ are plotted as white dots. In figure 3.1 B) we show for illustration an RP for the Rössler system (in figure 3.1 A)), which is a chaotic system described by three, nonlinearly coupled, first order ordinary differential equations [28].

Formally, for a phase-space orbit described by the time series of vectors $\vec{x}_i$, $i = 1, 2, \ldots$, in a proper embedding space, the RP matrix can be defined from the expression:

$$R_{i,j}(\epsilon) = \Theta(\epsilon - \|\vec{x}_i - \vec{x}_j\|), \tag{3.1}$$

where Θ is the Heaviside function. From this definition, we see that the RP has always a black main diagonal, since $R_{i,i} \equiv 1$. The threshold ϵ can be chosen as e.g. a few per cent of the maximum phase space diameter, or as a few standard deviation of the observational noise in the data. Patterns in RPs can be classified as follows:

- Homogeneous: Typical for stationary systems, where time spanned by the RP is longer than the typical scales of the system.
- Diagonal lines: Segments of trajectory recur and run together for some time, which is determined by the length of the diagonal line.

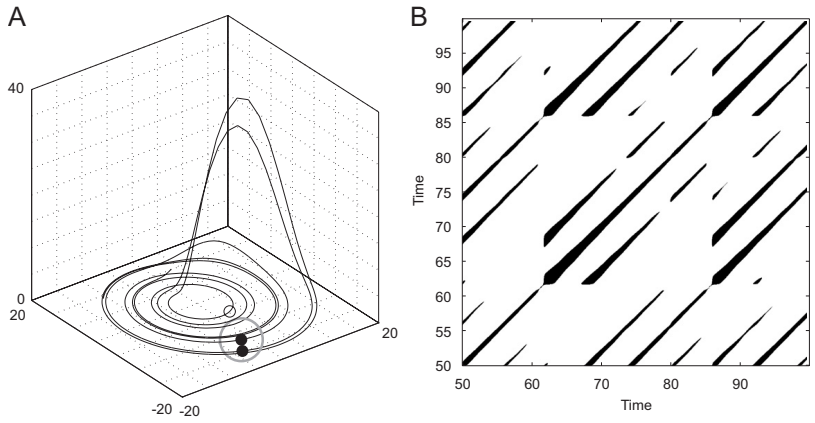

Figure 3.1: A) Rössler attractor, B) RP for Rössler system demonstrates recurrences of the trajectories

- Vertical and horizontal lines: Some states do not change or change slowly; indication of laminar states.
- White bands: Non-stationary data, transitions may have occurred, extreme events.
- Single isolated points: Strong fluctuations, uncorrelated random or anti-correlated process.
- Fading to the upper left and lower right corner: Non-stationary data; the process contains a trend.

One RP can exhibit many of the mentioned patterns simultaneously. For example, a chaotic system gives rise to single, isolated points as well as diagonal lines. Quasi-periodic systems, where ratios between frequencies in the system are irrational, can also have RPs that are indistinguishable from chaotic systems. In this case, the largest Lyapunov exponent should be computed, and if it is positive the system is chaotic. Periodic systems produce uninterrupted, diagonal lines and the distance between diagonal lines gives the period. In the case of noise or random processes RPs consist of mostly isolated, uniformly distributed points whose distances are also uniformly distributed, indicating that there is no predominant time scale in the system.

Generalizations, like cross-recurrence plots (CRP) can be defined [29], where the recurrences between the trajectories of two systems in the same phase space are considered:

$$CR_{i,j}^{\vec{x},\vec{y}}(\epsilon) = \Theta(\epsilon - \|\vec{x}_i - \vec{y}_j\|). \tag{3.2}$$

Also, joint-recurrence plot (JRP) can be used to compare the recurrences of the trajectory of two different systems in their respective phase spaces [30]:

$$JR_{i,j}^{\vec{x},\vec{y}}(\epsilon_x, \epsilon_y) = \Theta(\epsilon_x - \|\vec{x}_i - \vec{x}_j\|)\Theta(\epsilon_y - \|\vec{y}_i - \vec{y}_j\|), \tag{3.3}$$

where ϵ_x and ϵ_y are thresholds in two different phase spaces. The advantage of JR over CR is that it can be applied to physically different systems, whose phase spaces have different

dimensions, or where phase spaces are obtained from different physical variables. We have used both JR and CR to visualize correlations between plasma potential and electron density in Paper I.

Measures of complexity in RP

A number of complexity measures can be introduced, which quantify the small scale structure in RP. To see how these measures vary as a function of time, one can compute them in small windows (sub-matrices) and then move these windows along the main diagonal of the RP. A detailed review on RP quantification analysis can be found in Marwan et al. (2007) [31]. The *recurrence rate* measures the density of the recurrence points in the RP:

$$RR(\epsilon) = \frac{1}{N^2} \sum_{i,j=1} R_{i,j}(\epsilon), \tag{3.4}$$

and in the limit $N \to \infty$, RR is the probability that the state recurs to its ϵ-neighborhood in phase space. This definition corresponds to the correlation sum, as observed from equation (2.5). *Diagonal measures* are based on the histogram $P(\epsilon, l)$ of diagonal lines of length l:

$$P(l) = \sum_{i,j=1}^{N} (1 - R_{i-1,j-1})(1 - R_{i+l,j+l})) \prod_{k=0}^{l-1} R_{i+k,j+k}.$$

RP measures can be computed for every diagonal line separately, with distance τ from the main diagonal, for example, τ-recurrence rate can be obtained. This measure can be interpreted as a probability that a state recurs to its ϵ-neighborhood after τ time steps:

$$RR_\tau = \frac{1}{N - \tau} \sum_{i=1}^{N-\tau} R_{i,i+\tau}, \tag{3.5}$$

and can be considered as a generalized auto-correlation function. It contains information about the full phase-space orbit and not only for a single component of the system's trajectory. Also, a *trend* in the data can be defined as a linear regression coefficient over the τ-recurrence rate as a function of τ.

In Paper III we suggest that the average inverse of diagonal line lengths:

$$\Gamma \equiv \langle l^{-1} \rangle = \sum_l l^{-1} P(l) / \sum_l P(l), \tag{3.6}$$

can be used as a proxy for the largest Lyapunov exponent in deterministic systems, and this is demonstrated for the Lorenz system. There we also demonstrate that for a signal which is predominantly a fractional Brownian motion, Γ is related to the inverse of the selfsimilarity exponent h. Therefore, we can conclude that Γ is a universal measure of predictability: in a chaotic system, it is related to the largest Lyapunov exponent, while in a stochastic system it is related to the long-range memory effects.

As mentioned, there are a multitude of RP quantification measures that are beyond the scope of this thesis. For instance, from the RP correlation entropy, correlation dimension

and generalized mutual information can be defined if the system is ergodic, and these measures are not dependent on the embedding dimension if this dimension is sufficient to unfold the attractor. We also mention that various studies have shown that vertical structures in the RP can detect chaos-chaos transitions as well as intermittency and laminar states [32].

3.2 EMD analysis

Empirical mode decomposition (EMD) was developed by Huang et al. (1998) [33] and is based on the local scale separation of time series. The essence of the method is to identify the intrinsic oscillatory modes by their characteristic time scales in the data empirically, and then decompose the data accordingly. At every moment in time each mode has an instantaneous frequency, and to define this frequency the time series has to be decomposed into signals whose mean is close to zero, and equal (or differ at most by one) number of zero crossing and extrema [34]. When a time series exhibits these properties it is called an intrinsic mode function (IF), which is a pure oscillatory mode that bears amplitude and frequency modulations. IFs can be obtained through the sifting process, which is an adaptive process derived from the data and is explained in Paper III. The higher modes have fewer oscillations and the IF with highest mode number is called the residual R, which is usually a monotonic function. This residual does not have the characteristics of the other IFs, since the mean is usually not zero, and represents the trend in a data with nonzero mean.

By the above definitions, IFs are complete in the sense that their summation gives the original time series: $s(t) = \sum_{j=1}^{M} h_j(t) + R(t)$, where $h_j(t)$ represent the IFs. The number M of IFs for a time series of N data points is close to $\log_2 N$. IF components should be orthogonal, since they are defined from the difference between the signal and its local mean. However, the mean is defined through the maximal and minimal envelopes and it is not a mean of the signal itself. Therefore, some leakage exist, but it should be small [33]. EMD for the AMO signal shown in figure 2.3 is shown in figure 3.2, where higher IFs show periodicity on ~ 20 and ~ 60 years. When inspecting these plots it is important to notice the vertical scales to get the correct impression. The three lowest modes are plotted within a range of ± 0.5, while the higher modes are plotted in the range ± 0.2. This means that the fluctuations on annual scales and shorter, are substantial. A benefit of EMD method is that a mean is not required, and the only criteria needed are the locations of the local extrema. Without the need of the mean, EMD is spared of a troublesome step of removing the mean values for the large DC term in data with non-zero mean. Instantaneous frequencies for a particular IF $h_j(t)$ can be computed from the Hilbert transform of the IF:

$$Y_j(t) = \frac{1}{\pi} P \int_{-\infty}^{\infty} \frac{h_j(t')}{t - t'} \, dt', \tag{3.7}$$

where P indicates the Cauchy principal value. From the conjugate pair $h_j(t)$ and $Y_j(t)$ we form an analytical signal $Z(_j t)$ whose amplitude and phase can be defined from the Euler formula: $Z_j(t) = h_j(t) + iY_j(t) = a_j(t)e^{i\theta_j(t)}$, where a is the amplitude of IF mode. The instantaneous frequency can be defined as $\omega_j = d\theta_j/dt \Rightarrow \theta_j(t) = \int^t \omega_j(t') \, dt'$, and the

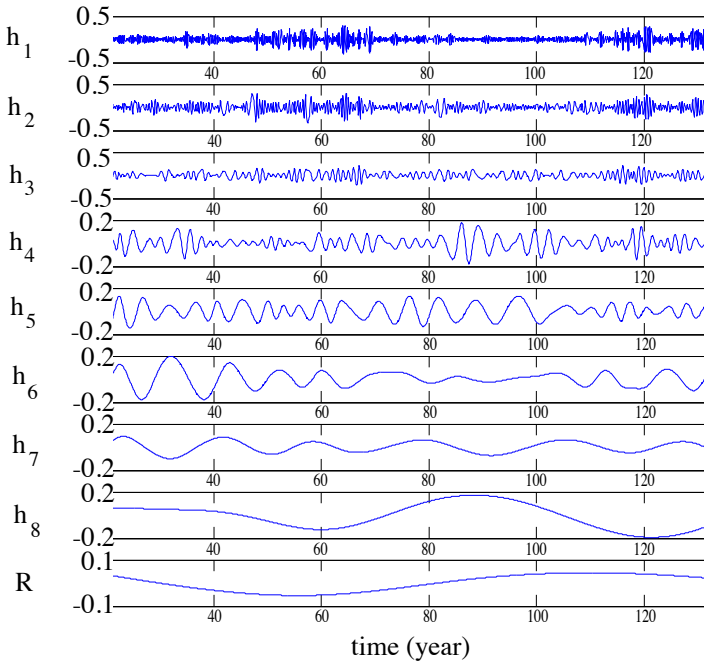

Figure 3.2: EMD for AMO signal.

energy of each IF is given as $H_j = \int^t a_j(t')^2 dt'$. It should be mentioned that the imaginary part $Y_j(t)$ could be produced with other methods than the Hilbert transform, but this transform defines imaginary part in such way that $Z_j(t)$ is an analytic function. We can now write the original signal as:

$$s(t) = \sum_{j=1}^{M} h_j(t) = \mathrm{Re} \sum_{j=1}^{M} (h_j(t) + iY_j(t)) = \mathrm{Re} \sum_{j=1}^{M} a_j(t) e^{i \int \omega_j(t) dt}, \tag{3.8}$$

where residual R is not included. The same data expanded in the Fourier representation would be

$$s(t) = \mathrm{Re} \sum_{j=1}^{M} a_j e^{i\omega_j t}. \tag{3.9}$$

Since, for each time t there exist an instantaneous energy $H_j(t) = a_j(t)^2$ and an instantaneous frequency $\omega_j(t)$, one can define Hilbert energy

$$H_j(\omega, t) = H_j(t)\delta(\omega - \omega_j(t)) \tag{3.10}$$

In figure 3.3 a) we have plotted such spectra for all IFs of the AMO signal as curves for $\omega_j(t)$ which are color coded to give the magnitude of $H_j(t)$ for each t.

Application of an adaptive basis, as done in EMD, has advantages over *a priori* chosen basis, since it does not introduce spurious harmonics to represent nonlinear waveforms.

3.3 Wavelet analysis

The wavelet analysis can be considered as an adjustable window Fourier analysis. The wavelet coefficients of a signal $X(t)$ are defined by the convolution integral

$$W(a,b;X,\psi) = |a|^{-1/2} \int_{-\infty}^{\infty} X(t)\psi^{\star}(\frac{t-b}{a})dt, \tag{3.11}$$

where $\psi^{\star}$ is a wavelet function, a is the time scale of a wavelet function, and b is the translation of its origin. Hence, b is the temporal location of the event, and $1/a$ is a frequency scale. Although one can make the wavelet orthogonal by selecting a discrete set of a, this discrete wavelet analysis will miss signals which have scales different from the selected discrete set of a. Wavelets for continuous a are not orthogonal. Wavelets are useful when there is a gradual frequency change in the data. In order to spot a change that occurred locally, one must look for the result in the high-frequency range, for the higher the frequency the more localized the basic wavelet will be. If a local event occurs only in the low-frequency range, one will still be forced to look for its effects in the high-frequency range. The other drawback compared to EMD analysis is the non-adaptive wavelet basis where the analyzing wavelet is chosen in advance. In this thesis, we use Mexican hat wavelet, which is from the class of continuous wavelets and is a second derivative of a Gaussian function.

In general, if more quantitative results are desired, the Hilbert energy spectrum presentation is better. If more qualitative results are desired, a wavelet presentation is better. In figure 3.3 a) we show Hilbert spectrum for AMO signal, while in figure 3.3 b) we plot mexican-hat wavelet coefficients for the same signal. We observe that both wavelet and Hilbert spectrum show increase in energy every 30 years or so, which is in agreement with the periodicity of the AMO signal. It also appears that the Hilbert spectrum gives more detailed information on the exact frequencies and times of the extremes in the AMO signal.

3.4 Test of determinism

This test was developed by Kaplan and Glass (1992) [35] and is extensively used in Paper III and Paper IV. It is based on the property of deterministic dynamical systems that the tangent to the trajectory is uniquely determined by the state vector, i.e. that phase space orbits in a properly chosen embedding space do not intersect. The embedded space is divided into boxes and a tangent vector is estimated as the difference between the embedded state vector at the exit and entrance of the box. If a trajectory recurs to the same box, its tangent is parallel to other tangents from the same box. The orientation vector for the kth pass through box j is the unit tangent vector $\mathbf{u}_{k,j} = \Delta\mathbf{x}_{k,j}(t)/|\Delta\mathbf{x}_{k,j}(t)|$. The estimated averaged displacement vector in the box is

$$\mathbf{V}_j = \frac{1}{n_j} \sum_{k=1}^{n_j} \mathbf{u}_{k,j}, \tag{3.12}$$

where n_j is the number of passes of the trajectory through box j. If the embedding dimension is sufficiently high and in the limit of vanishingly small box size, the trajectory

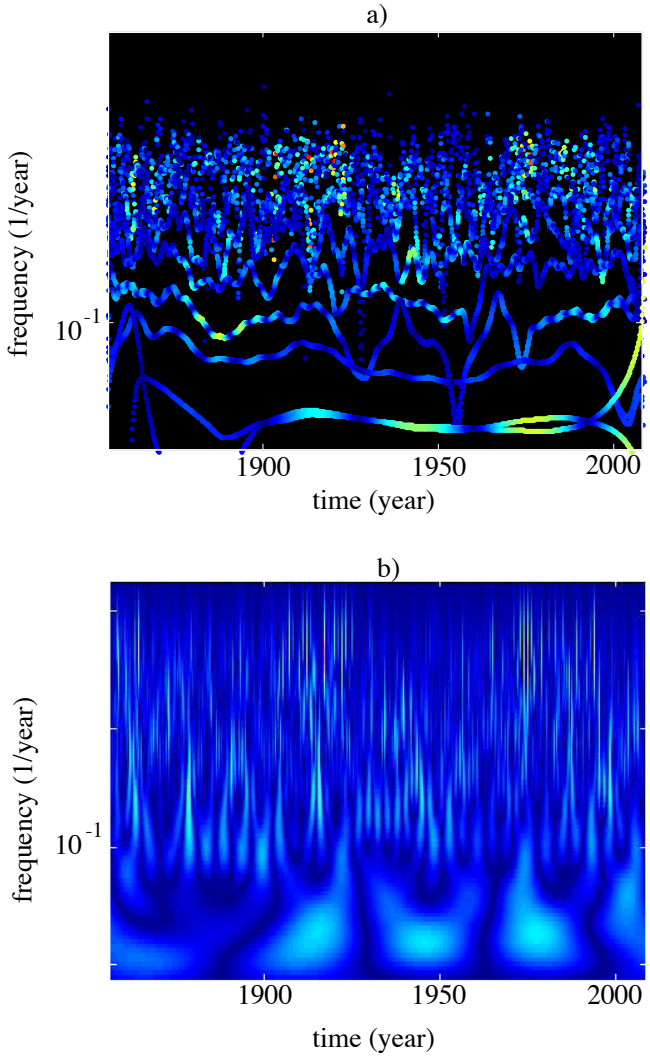

Figure 3.3: a) Hilbert spectrum for AMO, b) wavelet spectrum for AMO.

directions should be aligned and $V_j \equiv |\mathbf{V}_j| = 1$. For a stochastic system the tangents inside a box have arbitrarily orientations and their $V_j \to 0$ in the limit $n_j \to \infty$. When the trajectory passages n_j through the box is finite, $V_j \approx 1$ for a properly embedded deterministic system, while $V_j \sim n_j^{-1/2}$ for Brownian motion. This means that the dependence of V_j on n_j can be used to distinguish stochastic from deterministic dynamics. The qualifier *properly embedded* is important here. If the system is deterministic, but high-dimensional, we cannot in practice find an embedding space that spans the high-dimensional attractor, and then a box in embedding space can contain states that are far separated in the actual phase space. This makes the orientation vectors in a box have arbitrary directions and V_j versus n_j behaves more like a stochastic process. Thus this test of determinism is really a test of deterministic and low-dimensional dynamics against high-dimensional or stochastic dynamics. Model examples of systems generating such dynamics are the Lorenz system and the stochastic equation for the fractional Ornstein-Uhlenbeck process, respectively. These models are discussed in Paper III. An example of a high-dimensional system, whose attractor can be low-dimensional for certain parameters, is discussed in Paper IV.

Another measure to distinguish these classes of dynamics is to define a measure Λ which shows the deviation of V from the value it takes for a Brownian motion (as in Paper III). For a random signal, Λ decreases rapidly with increasing time-delay τ employed in the phase-space reconstruction in a random signal, but remains more or less constant with τ for a deterministic low-dimensional signal.

Yet another technique is to compare the measures $V_j(n_j)$ and $\Lambda(\tau)$ to the corresponding measures for a surrogate signal created by randomizing the phases of Fourier coefficients of the original time series. This works as a test for nonlinearity and low-dimensionality, since the measures will change significantly if the dynamics is low-dimensional and nonlinear. High-dimensional or stochastic dynamics does not seem to be sensitive to randomization of phases, and for fractional Brownian motions this is easily proven.

In Paper III and IV we have also studied different solar wind parameters and geomagnetic indices as well as some simple model systems. For instance, we have concluded that if V_j and/or Λ for a given signal is reduced after randomization of phases, the dynamics of the original signal has a low-dimensional and nonlinear component. Systems that we study in those papers are predominantly stochastic and therefore sometimes data have to be mildly low-pass filtered before application of the test. Otherwise the test may not be able to discern the low-dimensional component. Some examples of $\Lambda(\tau)$ will be shown in chapter 4.

3.5 PVD analysis

The principal value decomposition (PVD) analysis method is also known as empirical orthogonal function expansion [36]. Here, the basis is not *a priori* prescribed. First, we form the covariance matrix $R = F^t F$, where F is a matrix where variable changes in both time (along the rows) and space (along the columns). Further, we solve the eigenvalue problem $RC = C\Lambda$. Here Λ is a diagonal matrix containing the eigenvalues λ_i of R, while the columns of C are the eigenvectors $\vec{c}_i$ of R. Each of these eigenvectors can be regarded as a map. This transformation is defined in such a way that the first eigenvector has as high

a variance as possible, i.e. it accounts for as much of the variability in the data as possible. Each succeeding component in turn has the highest variance possible under the constraint that it has to be orthogonal to the preceding components. Also, $C^tC = CC^t = I$, meaning that eigenvectors are uncorrelated over space. Further, we can obtain the time evolution of the eigenvector $\vec{a}_i = F\vec{c}_i$, which is also called a *principal component time series*. As $\vec{c}_i$ are uncorrelated in space, $\vec{a}_i$ are uncorrelated in time. A disadvantage of this method is that it only gives the distribution of the variance in the eigenmodes, but it does not suggest scales of frequency content of the signal. The method is often used in climate studies as the data is a function of both space and time. This is demonstrated in chapter 4. In Paper I singular value decomposition (SVD) is also used, which is similar to PVD, but unlike PVD which is applied to the ensemble of measurements, SVD is applied to a single set.

Chapter 4

Applications

In this chapter concepts and methods described in the previous chapters are employed to analyze data from a plasma Helimak experiment, where low-dimensional chaos is observed (in Paper I and Paper II), and for the magnetosphere, where dynamics is analyzed during geomagnetic storms and substorms (Paper III and Paper IV). In addition, we analyze data from a laboratory plasma in the simple magnetized torus configuration and compare dynamics on different time scales. Finally, some climate indices are analyzed and the results are discussed from a complex-system perspective.

4.1 Laboratory plasma

In Paper I and Paper II plasma potential and electron density fluctuations from the Blaamann device in Helimak configuration are examined. As pointed out in [37] the Helimak is a device suitable for studies of low-frequency gradient driven instabilities and their routes to turbulence in the presence of magnetic field curvature. Also, it is the simplest toroidal plasma configuration that permits a magnetohydrodynamic equilibrium. Plasma with a confining magnetic field in the toroidal direction is not in equilibrium since charge dependent gradient B and curvature drifts lead to an electric field which further produces $E \times B$ drift. However, when a small vertical magnetic field is imposed, as in the case of Helimak configuration, short-circuiting currents are produce that limit the electric field [38]. When the magnetic field in Helimak configuration is increased the plasma approaches a turbulent regime at low frequencies, perhaps through a period-doubling route. By measuring cross coherence and cross phase as a function of vertical displacement, flute modes are discovered on the low field side of the electron density profile [37]. The flute mode number locks itself to a single mode which further indicates that the wave field could be represented by a low-dimensional set of autonomous differential equations. Paper I examines the existence of low-dimensional chaotic component in signals from plasma potential and electron density. These signals are smoothed by a moving average filter in order to study the global oscillations of the background plasma. We show by means of mean-field dimensional method [39] that the correlated database of filtered plasma potential and electron density is low-dimensional, and that the largest Lyapunov exponents for both signals are positive, implying low-dimensional chaos. Recurrence plots, cross recurrence plots, and joint recurrence plots are also used and they all suggest chaotic behavior inside entire

plasma chamber.

Paper II shows similarities in the time evolution of the filtered electron density and diffusionless Lorenz equations. Filtered electron density is used in order to study the dynamics of the background plasma and ignore simple $E \times B$ dynamics of the convection cells. An animation of filtered electron density shows standing wave with random phase shifts. Power spectra, recurrence plots, and Lyapunov exponents are compared for diffusionless Lorenz equation and filtered electron density, and these properties are shown to be very similar in both cases, implying that low-dimensional chaos in the plasma device could be described by the diffusionless Lorenz equation.

Below, we present some findings from the Blaamann device in the simple magnetized torus configuration. Here the plasma is generated by a hot filament discharge in a plasma torus with a purely toroidal magnetic field (no poloidal or vertical field component). On the low-field side (LFS) of the torus cross section the electron pressure gradient is directed in the opposite direction of the radius of curvature vector of the magnetic field, and the plasma is unstable to the electrostatic flute interchange instability here. Since hot electrons are injected through the filament in the center of the torus cross section there will be a potential minimum in the center, and this makes the plasma rotate poloidally by $\mathbf{E} \times \mathbf{B}$ drift (see figure 4.1). This rotation velocity increases with decreasing neutral gas pressure, and for low neutral pressures the lowest poloidal mode number dominates to give a well defined peak in the power spectrum of signals. The frequency of this peak corresponds to the rotation frequency f_{rot}. For high neutral pressure the rotation frequency is smaller than the characteristic time for growth and nonlinear cascading of the flute modes, so this "turbulent" regime can be observed for $f \geq f_{rot}$. The spectrum for $f \ll f_{rot}$ is associated with global fluctuations of the plasma state, and can be considered as nonlinear oscillations in an electric circuit where the plasma plays the role of a strongly nonlinear circuit element. Fluctuations in plasma potential and electron density measured by electrostatic probes in the middle of the pressure slope on the LFS are shown in figure 4.2. The signals are sampled at 100 kHz, i.e. the sampling time is $\Delta t = 10$ μs. The plasma rotation period of 2 ms thus corresponds to $200\Delta t$ and is seen as a weak bump at 0.5 kHz on the potential power spectrum in figure 4.3, and as a stronger bump on the electron density spectrum. The most prominent feature observed by direct examination of the signals in figure 4.2 is the prominant spikes occuring with interspike intervals ranging from $20 - 200$ Δt. This time range corresponds to the plateaus observed in the frequency range $0.5 - 5$ kHz in figure 4.3. The spikes are very peaked, with width $< 20\Delta t$. These time scales correspond to the power-law tail $S(f) \sim f^{\beta}$ of the spectra for $f > 5$ kHz, with $\beta \approx 2.5$. The flat plateaus in the spectra in the frequency range $0.5 - 5$ kHz reflect the white-noise character of the distribution of the spikes, and are similar for potential and density. In fact, the larger potential and density peaks are correlated, positive density spikes are associated with negative potential spikes, as they should for flute modes. For frequencies below 1 kHz the electron density spectrum (apart from the rotation hump) has a more or less flat white noise like spectrum, whereas the potential has a power-law range for $0.1 < f < 1$ kHz with $\beta \approx 1.4$, which is indicative of a strongly antipersistent self-affine motion. Since these low-frequency fluctuations are not present in the electron density spectrum, and are on frequencies below the plasma rotation frequency, they are not associated with flute-mode turbulence, but rather to global oscillations, as mentioned above. For frequencies below 0.1

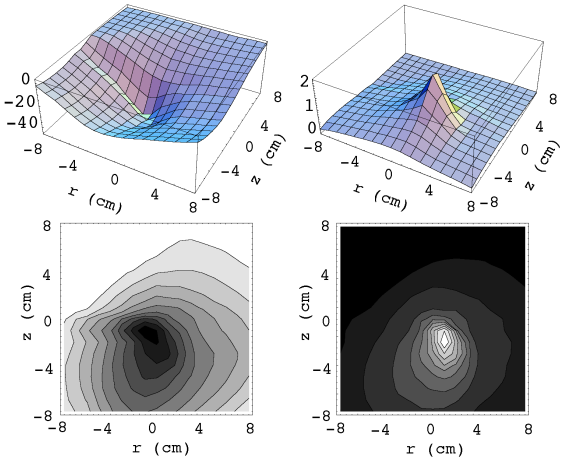

Figure 4.1: Left: potential profile through a poloidal cross-section of the torus. The plasma flows by $\mathbf{E} \times \mathbf{B}$-drift along the equipotential lines, Right: electron density profile. Because of the toroidal magnetic field curvature electrostatic flute modes are unstable on the low-field side, i.e. on the outer slope of this profile (in the right half of the figure on the low right).

kHz this spectrum becomes flat, indicating a white-noise like process with complete loss of temporal correlation on time scales longer than 10 ms ($1000\Delta t$).

The probability density functions (PDFs) of differences in potential and density separated by a time interval τ is shown for varying τ in figure 4.4 a) and figure 4.4 c). Both distributions are leptokurtic for small τ, but while the electron density rapidly converges towards a near-gaussian shape (which has kurtosis $K = 3$), the plasma potential converges to a leptokurtic distribution with $K \approx 10$, as shown in figure 4.5 a). The increasing kurtosis at small scales is a fundamental statistical signature of intermittency.

On the long time scales, where the signals have a stationary character, it makes more sense to consider the PDFs of the coarse grained signals [40]. Such signals are made by running averages over intervals of length τ. PDFs for increasing degrees of coarse-graining are shown in figure 4.4 b) and figure 4.4 d), and show a near-gaussian distributions for density, while the potential maintains a leptokurtic and strongly skewed distribution throughout the scales corresponding to frequencies $f > 0.1$ kHz. These PDFs maintain relatively constant shape through the scales corresponding to the power-law frequency range $0.1 < f < 1$ kHz, and hence the signals have a self-affine character in this range. In the range $f < 0.1$ kHz the signals are more gaussian-like, and have the character of gaussian white noise.

The rapid fall of kurtosis in figure 4.5 a) occurs over time scales $\tau < 2^5$, corresponding to frequencies in the power-law tail of the spectrum. This is the time scale of the peaks of the spikes, and thus the drop of the kurtosis (intermittency) is a property that characterizes the shape and distribution of these spikes.

So far, what we know about the low-frequency fluctuations is that they are uncorrelated and near-gaussian. It would be interesting to know if they should be considered as stochas-

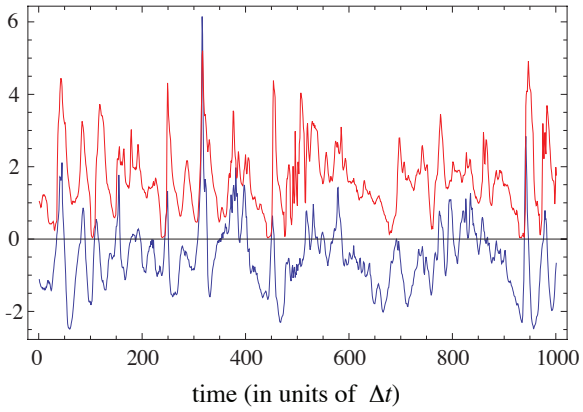

Figure 4.2: Upper trace (red) is the time series of electron density fluctuations. Lower trace (blue) is the same for (sign-inverted) plasma potential. Units are arbitrary, and the plasma potential has an arbitrary zero potential.

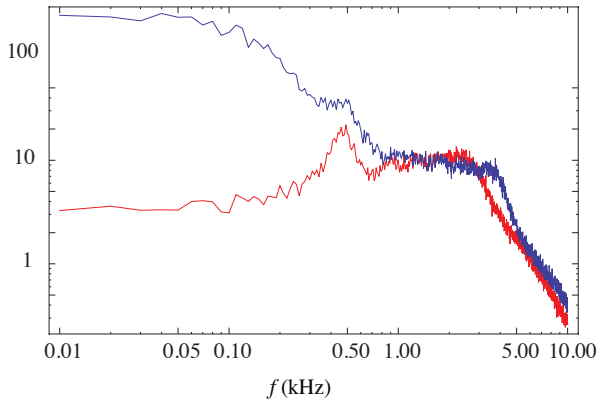

Figure 4.3: Log-log power spectra for electron density (lower red curve) and for plasma potential (upper blue curve).

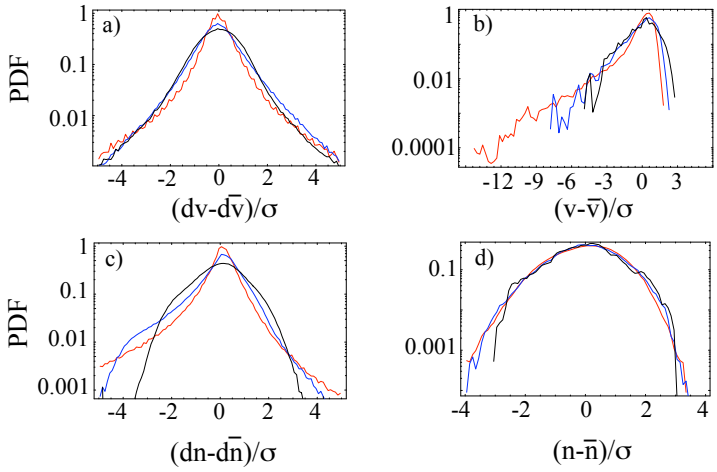

Figure 4.4: Logarithmic plots of PDF for a) differences in plasma potential separated by time τ, where red is $\tau = 2^0$, blue is $\tau = 2^3$ and black is $\tau = 2^6$; b) coarse-grained plasma potential averaged over interval τ, where red is $\tau = 2^8$, blue is $\tau = 2^{11}$ and black is $\tau = 2^{14}$; c) differences in the plasma density, where red is $\tau = 2^0$, blue is $\tau = 2^3$ and black is $\tau = 2^6$ (larger scales are the same as $\tau = 2^6$); d) coarse-grained electron density, where red is $\tau = 2^8$, blue is $\tau = 2^{11}$ and black is $\tau = 2^{14}$. Time τ is in units of Δt.

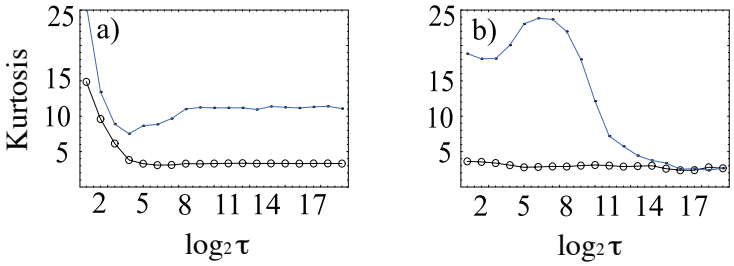

Figure 4.5: a) Kurtosis for differences in plasma potential separated by time τ (dotted line) and for differences in electron density (open circles). b) Kurtosis for coarse-grained plasma potential averaged over interval τ (dotted line), and for coarse-grained electron density (open circles).

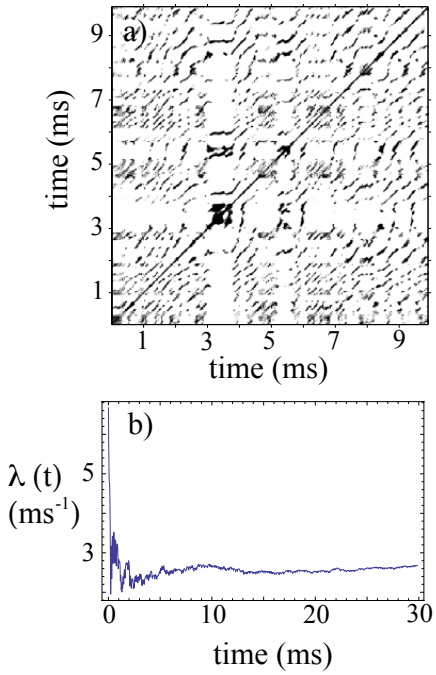

Figure 4.6: Chaotic characteristics of the filtered plasma potential: a) Recurrence plot, b) Lyapunov exponent.

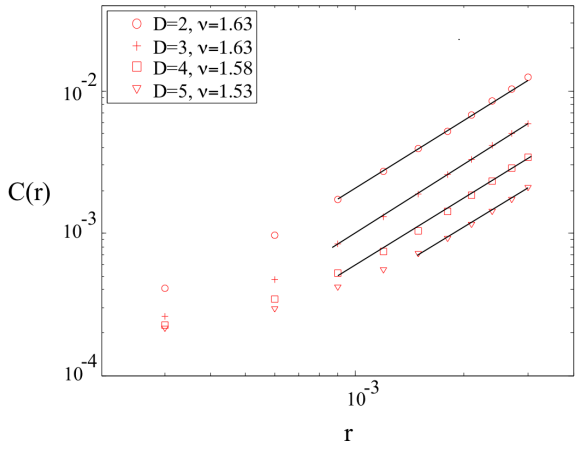

Figure 4.7: Log-log plot of correlation integrals $C(r)$ for embedding dimension $D = 2, 3, 4, 5$. The full lines are linear fits to the curves, which all have slopes $\nu \approx 1.6$.

tic, or if they may be a result of low-dimensional chaotic dynamics. For this purpose we apply a mexican hat wavelet filter on the plasma potential in order to extract the dynamics on scales larger than the poloidal rotation time, and hence wavelet coefficients corresponding to frequencies larger than the rotational frequency are set to zero by the filter. We have not done the same analysis for the electron density, since its spectral power is very low on the largest scales. Prior to the following analysis, the phase space is reconstructed by time-delay embedding (equation 2.3). Time-delay τ should be large enough such that reconstructed vectors do not depend on each other, and contain a new piece of information each. However, since chaotic systems are intrinsically unstable, if τ is too large, it may happen that vectors will become random in respect to each other and independent in statistical sense. In our analysis, τ is estimated from the first minimum of the average mutual information function [41], which is the most optimal method for the time-delay calculation in the time series whose underlying dynamics might be nonlinear.

For the low-pass filtered plasma potential we compute the largest Lyapunov exponent λ for the embedding dimension $M = 6$ and $\tau = 5$. In figure 4.6 b), the largest Lyapunov exponent is plotted as a function of time, and converges to $\lambda(t) \sim 2 \times 10^{-3}$ s^{-1}. However, it has been shown in [42] that stochastic time series can also give positive Lyapunov exponents when calculated numerically. Therefore, we apply RP analysis in order to visualize the phase space, for the embedding dimension $M = 6$ and $\tau = 5$. In figure 4.6 a), we see that the low-pass filtered plasma potential fluctuations exibit chaotic signatures.

In order to determine the correlation dimension of the chaotic attractor, we first calculate the modified correlation integral

$$C(r, W) = \frac{2}{N^2} \sum_{n=W}^{N} \sum_{i=1}^{N-n} H(r - |\mathbf{x}_{i+n} - \mathbf{x}_i|)$$

introduced in [43]. Here W is approximately equal to the autocorrelation time τ of the time series. When $W = 1$, the modified integral reduces to the Grassberger- Procaccia correlation integral, introduced in equation (2.5). Here, $C(r, W)$ is used in order to discard the influence of the time correlations in the correlation integral. It has been shown in [44] that the time series with a signature of a colored noise can also give low correlation dimension. On the other hand, when $W > \tau$, points close in time are removed from the correlation integral. We, further, calculate the correlation dimension ν from $C(r, W) = r^{\nu}$ for various $r < A$. Here, A is the maximum radius of the underlying strange attractor. For the low-pass filtered potential, we make a log-log plot of $C(r, W)$ vs. r for the embedding dimensions $M = 2, 3, 4$ and 5 in figure 4.7. As one can see, the correlation dimension changes very little for different M, which further implies that the unfolding of the phase space does not influence the dimension of the attractor in the phase space. The natural conclusion is that the trajectories all lay on the strange attractor, which has a fractal dimension $\nu \approx 1.6$, and hence the low-pass filtered potential has low-dimensional, chaotic dynamics.

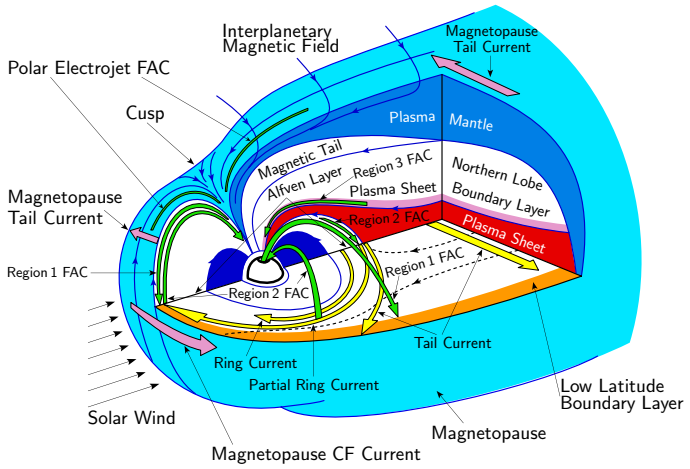

Figure 4.8: Magnetospheric currents (picture is taken from Feldstein et al. (2006) [45].)

4.2 Magnetosphere

The solar wind is a flow of magnetized plasma originating on the Sun. It flows with a speed of about 400 $\mathrm{km} s^{-1}$, and carries a magnetic field of about 5 nT. When the solar wind "collides" with the dipole magnetic field of the Earth, the elongated magnetospheric cavity is formed as shown in figure 4.8. This cartoon depicts the electric current systems in the magnetosphere, which is a result of the solar wind-magnetosphere interaction, some of which are closed via currents flowing in the partly ionized ionosphere.

Both the solar wind and the magnetosphere are subject to considerable variability, and both are bursty in nature. These bursts can crudely be divided into two main classes: magnetic storms (analyzed in Paper III) and substorms (analyzed in Paper IV). A substorm is an abrupt increase in nightside hemispheric auroral power [46], and the event occurs across the entire width of the magnetotail. This process requires major topological reconfigurations. The visual consequence of the substorm is the polar aurora, which appears due to enhanced electron and proton preciptation along the magnetic field lines, which are related to enhanced currents in the Earth's ionosphere, for instance the auroral electrojet currents. During the substorm event also field aligned currents are formed or intensified. The duration of substorms are at most a few hour, while magnetic storms can last for days. Storms are often directly correlated to identifiable eruptions on the Sun and they typically activate other current systems of the magnetosphere, like the equatorial ring current [47]. This implies that different geomagnetic indices are sensitive to substorms and storms.

The conjecture that the magnetosphere-ionosphere system resides in an SOC state has been inferred from the satellite measurements in the inner plasma sheet [48], from geomagnetic indices (whose reliability is discussed in [49]), from the measurements seen by UVI auroral imagers on satellites [50] or from ground-based all-sky cameras [51]. This

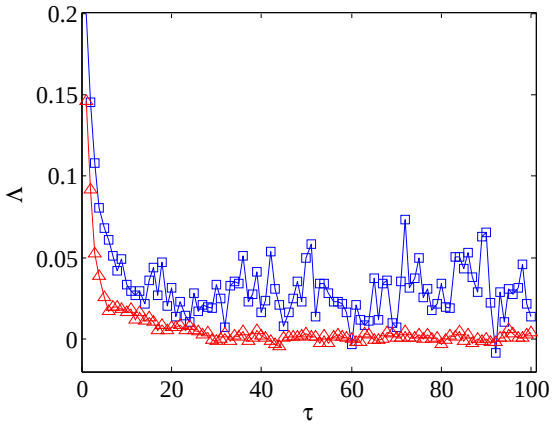

Figure 4.9: $\Lambda(\tau)$: blue squares are derived from the AE index, red triangles from the same signal after randomization of phases of the Fourier coefficients.

illustrates how data from widely different souces can be analyzed and synthesized to form a global picture of the dynamics of the magnetosphere. Chapman et al. (1998) [52] have preposed a model where SOC dominates internal dynamics of the magnetosphere, whereas energy dissipated on the systemwide scales (during substorm events) follows a probability distribution with a well defined mean. A characteristic feature of the magnetosphere is the abundance of physical mechanisms operating on widely different time scales. For instance, the time it takes to load energy into the magnetosphere tail is 10-20 minutes. On the other hand, the substorm onset time is of the order one minute and is determined by the Alfvén bounce time to the ionosphere. This wide separation of scales, and the power-law distribution between them, is often taken as a support of SOC dynamics in the magnetotail, as dicussed in Angelopoulos et al. (1999) [48]. Also in [48], signatures of intermittent turbulence were observed, which gave support to the interpretation that the physical mechanism behind SOC is the cross-tail intermittent turbulence which transfers momentum and mass when a certain threshold is exceeded.

However, it was pointed out by Consolini and Chang (2001) [53] that in the case of classical SOC the critical state is resilient with respect to variations of the external driving, while the Earth's magnetosphere seems to be rather sensitive to such variations. That is why, according to the same authors, the observed criticality in the magnetosphere could have been "forced" and not always "self-organized" criticality. Another conjecture for explaining the magnetospheric complexity was proposed by Sitnov et al. (2001) [54], who suggested that the magnetosphere undergoes a first order phase transition during substorms, and that the general scale invariance can be explained by assuming that the magnetosphere resides close to the critical point of a second order phase transition.

In Paper IV we test for changes in determinism of magnetospheric dynamics during substorms. There we compute $V_j(n_j)$ for the auroral electrojet (AE) index and its randomized version, and the result suggests that the AE index exhibits a low-dimensional, nonlinear component. Similar is shown in figure 4.9 for Λ versus time-delay τ. This observation has been made also by other authors (for example, [55], [56]), but here we obtain this result

without relying on any filtering procedure. Further, our analysis presents evidence that low-dimensionality is common also for other geomagnetic indices under substorm conditions. A similar study is made in Paper III for magnetic storms, where we are able to demonstrate that the magnetosphere becomes more low-dimensional and nonlinear during individual magnetic storms.

The main difference between magnetic substorms and storms revealed by these studies seems to be increased predictability in both solar wind and magnetosphere during storms, which is not observed during substorm conditions.

The obvious interpretation of these results is that global instabilities of the magnetosphere makes it more organized since the effective degrees of freedom decreases because of the collective behavior. In Paper III and Paper IV no corresponding organization is seen in the solar wind parameters, which means that magnetosphere *self*-organizes during magnetic disturbances.

In Paper IV a simple stochastic equation is proposed as a minimal model for the global dynamics the magnetosphere. This equation has a nonlinear damping and multiplicative noise term, which makes it one-dimensional and nonlinear when the noise is filtered out. Test of determinism gives very similar results for low-pass filtered output of this equation and for filtered AE index. Also, power spectra of the AE index and the output of this equation are rather similar, demonstrating that simple dynamic-stochastic models can reproduce some of the essential statistical properties of global magnetospheric dynamics including substorm activity. However, in order to produce observed characteristics of the geomagnetic indices, more refined models need to be made. Interesting discussion on models for magnetospheric dynamics can be found in Watkins et al. (2001) [57].

4.3 Climate

In this section, we discuss some stochastic equations that have been used to describe different climate processes. Towards the end, we perform a test of determinism to some climatic indices and discuss the results.

Sea surface temperature (SST) is the most important characteristic of oceans. It is governed by both atmospheric (wind speed, air temperature, cloudiness, and humidity) and oceanic (heat transport by currents, vertical mixing, and boundary layer depth) processes. SST variability can be described through the stochastic climate model paradigm, where ocean temperature anomalies are forced by random atmospheric variability, i.e. the ocean layer integrates the white noise atmospheric forcing to yield a red noise SST response [58]. Therefore, the persistence of SST anomalies is limited to the timescale associated with thermal inertia of the ocean layer and slow SST variations may be induced by random atmospheric forcing simply due to the thermal inertia associated with the ocean.

The spatial structures of large-scale patterns (e.g. the North-Atlantic oscillation) of extratropical atmospheric circulation variability are driven by processes intrinsic to the atmosphere and require no external forcing to exist. The temporal evolution of these atmospheric circulation patterns is generally consistent with a stochastic first-order autoregressive process (see [59]). In contrast to the extratropics, large-scale patterns of atmospheric variability in the tropics result primarily from interaction with the ocean as in

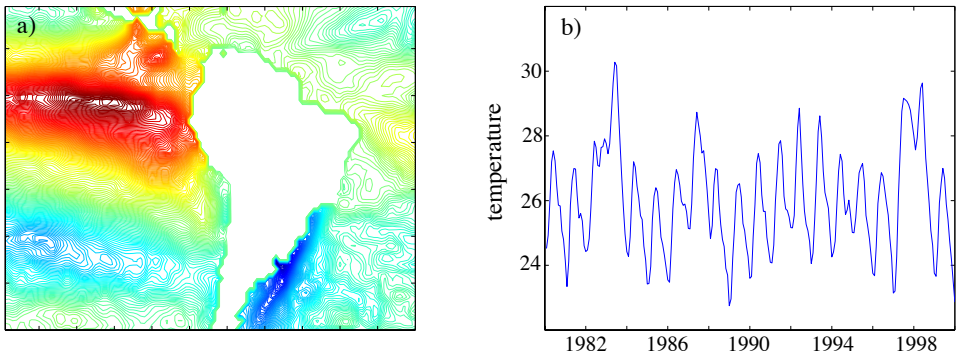

Figure 4.10: a): The first PVD component of SST, b): Time series of the first PVD component (temperature is in degrees Celsius).

the case of the El Niño Southern Oscillation (ENSO).

The leading PVD component of monthly SST anomalies over the globe is the ENSO mode, which causes large temperature variations in the tropical Eastern Pacific ocean and air surface pressure changes in tropical Western Pacific in the winter period. ENSO intensifies every 3-7 years, and can last as such between nine months to two years. It causes floods, droughts and other weather disturbances in many regions over the globe. In figure 4.10 a) we plot the leading PVD of the SST in period between 1980-2008. The SST data set is downloaded from **http://badc.nerc.ac.uk/data/hadisst/**; it is in situ/satellite data, collected monthly and with a $1^\circ \times 1^\circ$ resolution. It appears that the highest SST is along the coast of Peru, corresponding to the ENSO mode. Also, in figure 4.10 b) we show a principal component time series for the leading PVD. The increase in SST can be seen around 1983 and 1998, which are the years of strong ENSO events. This means that the greatest variability in the SST over the globe is due to the ENSO event.

SSTs in the North Atlantic undergo slow variations with a period on the order of 65-80 years, which is coined the Atlantic multidecadal oscillation (AMO), which we analyzed in section 2.3. The AMO is associated with large-scale precipation changes and with a frequency of severe Atlantic hurricanes. Modeling studies indicate that this mode is intrinsic to the ocean and stochastically forced by the atmosphere [60]. A delay differential equation which has been very successful in describing the nature of the ENSO was proposed by Ghil et al. (2008) [61]:

$$\frac{dh(t)}{dt} = -a\tanh[kh(t-\tau)] + b\cos(2\pi\omega t). \tag{4.1}$$

Here $h(t)$ represents the thermocline depth deviation from the annual mean in the Eastern Pacific . The delayed negative feedback does not let a solution fade away or be unstable, and creates an internal oscillator with period depending on the delay. However, a delayed oscillator typically has periodic solutions with well defined periods, while the occurrence of ENSO event is irregular. Also, phase-locking during the winter cannot be explained by a purely internal delayed oscillator. These discrepancies can be removed by considering nonlinear sigmoid type of interactions between the internal oscillator and the external

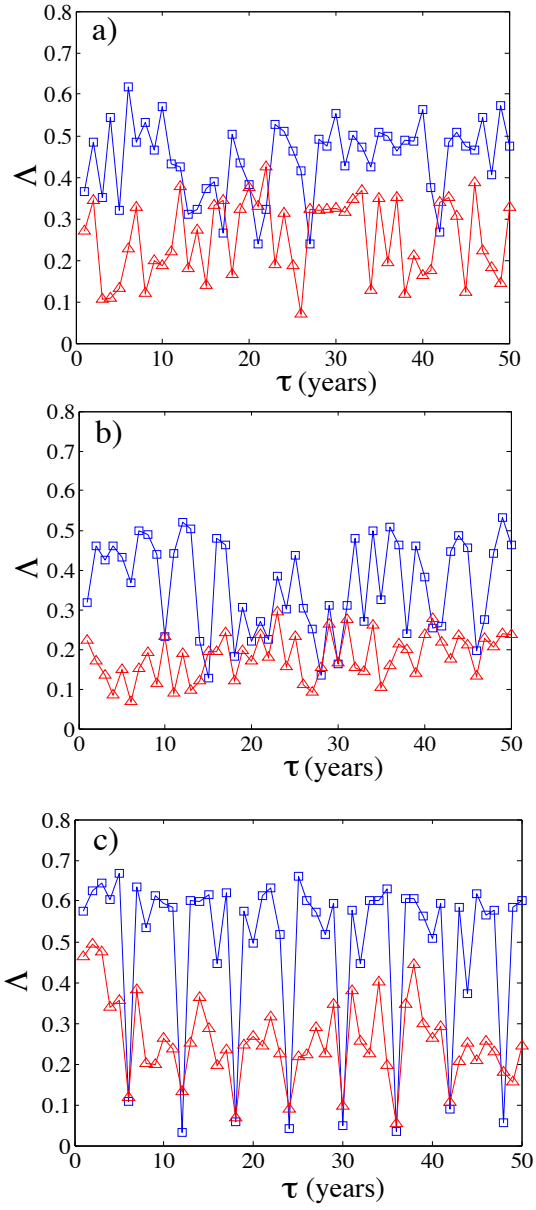

Figure 4.11: $\Lambda(\tau)$: a) filtered AMO, b) filtered temperature, c) NiNO3. Blue squares are derived from the original time series, red triangles from the same signal after randomization of phases of the Fourier coefficients.

periodic forcing by the seasonal cycle [62]. The increase of solution complexity from periodic to chaotic is caused by the increase of the atmosphere-ocean coupling parameter.

We compute $\Lambda(\tau)$ for low-pass filtered AMO, global temperature, and NiNO3 data. The latter measures the strength of an ENSO event and is defined as the SST anomaly averaged over the eastern equatorial Pacific. It was shown in [63] that $\Lambda(\tau)$ as a function of embedding dimension m does not increase for linear, stochastic systems, while it increases otherwise. We use relatively high embedding dimension $m = 10$ in order to obtain greater difference in $\Lambda(\tau)$ for the index and its randomized version. Since these indices are available since late $19th$ century and have only monthly resolution, the number of data points is around two thousand. Hence, further increase of m would give us bad statistics. Results are plotted in figure 4.11. We see that $\Lambda(\tau)$ for all indices is elevated compared to their randomized versions, implying that there is a low-dimensional, nonlinear component in each of these processes, even though in AMO and the global temperature it is obvious only after filtering. We observe that these two indices overlap with their randomized versions for some time periods, which might indicate a dominance of stochastic forcing or bad statistics. A more detailed study of AMO and global temperature is needed to make further conclusions.

That ENSO is elevated above its randomized version without the need of filtering indicates that it is a highly deterministic process that could be possibly described by equation (4.1). However, during intense ENSO episodes, which repeat on the average every 6 years, its deterministic nature decreases. This indicates that some stochastic, atmospheric forcing might be dominant on these time scales. Therefore, equation 4.1 should also contain some stochastic terms. The difference of $\Lambda(\tau)$ between ENSO and its randomized version also indicates that ENSO can not be explained as a linear, stochastic model.

This section has given wide range of possible studies of climate that we will examine in more details in the future.

4.4 Paper 1:

Evidence of low dimensional chaos in magnetized plasma turbulence

Eur. Phys. J. Special Topics, **164**, *157, 2008*

4.5 Paper 2:

Experimental evidence of low-dimensional chaotic convection dynamics in a toroidal magnetized plasma

Phys. Rev. E, **77**, *2008*

4.6 Paper 3:

Low-dimensionality and predictability of solar wind and global magnetosphere during magnetic storms

submitted to Journal of Geophysical Research

4.7 Paper 4:

Organization of the magnetosphere during substorms

submitted to *Journal of Geophysical Research*

Bibliography

[1] Sornette, D., Critical Phenomena in natural sciences: Chaos, Fractals, Selforganization and disorder: Concepts and tools, Springer-Verlag Berlin, (2000).

[2] Sprott, J. C., Chaos and time-series analysis, Oxford University Press, (2003).

[3] Hilborn, R. S., *Chaos and nonlinear dynamics* (2nd edn.), Oxford University Press, (2000).

[4] Ruelle D., *Chaotic evolution and strange attractors*, Lezioni Lincee, edited by Luigi A. Radicati di Brozolo, Scuola Normale Superiore, Pisa, (1989).

[5] Takens, F., *Detecting strange attractors in turbulence*, In Dynamical Systems and Turbulence , edited by D. A. Rand, and L. S. Young, Springer, New York, **898**, 366-81, (1981).

[6] Romanazzi, N., M. Lefranc and R. Gilmore, *Embeddings of low dimensional strange attractors: Topological invariants and degrees of freedom*, Physical Review E **75**, 066214, (2007).

[7] Casdagli, M., *A dynamical system approach to modelling input-output systems*, in Nonlinear Modeling and Forecasting, edited by M. Casdagli and S. Eubank, Addison-Wesley, **12**, 265, (1992).

[8] Broomhead, D. S., and G. P. King, *Extracting qualitative dynamics from experimental data*, Physica D **20**, 217, (1986).

[9] Whitney, H., *Differentiable Manifolds*, Annals of Mathematics **37**, 645, (1936).

[10] Grassberger, P., and I. Procaccia, Physical Review Letters **50**, 5 (1983).

[11] Osborne, A. R, and A. Provenzale, *Finite correlation dimension for stochastic systems with power-law spectra*, Physica D **35**, 357, (1989).

[12] Haken, H., *At least one exponent vanishes if the trajectory of an attractor does not contain a fixed point*, Physics Letters A **94**, 71, (1983).

[13] Ghorui, S., S. N. Sahasrabudhe, P. S. S. Murthy, A. K. Das, N. Venkatramani, *Estimation of dynamic properties of attractors observed in hollow copper electrode atmospheric pressure arc plasma system*, Pramana joirnal of physics, **59**, pp. 143, (2002).

[14] Beran, J ., Statistics for long-memory processes, *Monographs on statistics and applied probability*, Chapman& Hall/CRC, Boca Raton, (1994).

[15] Malamud, B. D, and D. L. Turcotte, *Self-affine time series I: Generation and analysis*, Advances in Geophysics, **40**, p. 1-90, (1999).

[16] Ivancevic, V. G., and T. T. Ivancevic, *Complex nonlinearity: Chaos, Phase transitions, topology change and path integrals*, Springer, (2008).

[17] Bak, P., C. Tang, and K. Wiesenfeld, *Self-organized criticality: An explanation of 1/f noise,* Physical Review Letters, **59**, 381, (1987).

[18] Jaeger, H. M., C. H. Liu, and S. R. Nagel, *Relaxation at the angle of response*, Physical Review Letters, **62**, 40, (1989).

[19] Aschwanden, M. *Self-organized criticality in astrophysics: The statistics of nonlinear processes in the Universe*, Springer Berlin, (2011).

[20] Vespignani, A., and S. Zapperi, *How self-organized criticality works: a unified mean-field picture*, Physical Review E, **57**, 6345, (1998).

[21] Turcotte, D., *Fractals and chaos in geology and geophysics*, Cambridge University Press, (1992).

[22] Bak, P., and C. Tang, *Earthquakes as a self-organized critical phenomenon*, Journal of Geophysical Research **94**, 15635, (1989).

[23] Carreras, B. A., D. E. Newman, E. Lynch, and P. H. Diamond, *A model realization of self-organized criticality for plasma confiment*, Physics of Plasmas **3**, 2903, (1996).

[24] Mandelbrot, B. B., *Fractals and scaling in finance: Discontinuity, Concentration, Risk*, Springer, New York, (1997).

[25] Roberts, D. C., and D. L. Turcotte, *Fractality and self-organized criticality of wars*, Fractals **6**, 351, (1998).

[26] Marwan, N., J. Kurths, and N. Wessel, *Recurrence plot based measures of complexity to predict life-Threatening cardiac arrhythmias*, Proceedings ECCTD, (2003).

[27] Trulla, L. L, A. Guliani, J. P. Zbilut, and C. L. Webber, Jr., *Recurrence quantification analysis of the logisitc equation with transients*, Physics Letters A **223**, 255, (1996).

[28] Rössler, O. E., *An equation for continuous chaos*, Physics Letters A, **57**, 397, (1976).

[29] Marwan, N., and J. Kurths, *Nonlinear analysis of bivariate data with cross recurrence plots*, Physics Letters A **302**, 299, (2002)

[30] Romano, M. C., M. Thiel, J. Kurths, W. von Bloh, *Multivariate recurrence plots*, Physics letters A **330**, 214, (2004).

[31] Marwan, N., M. C. Romano, M. Thiel and J. Kurths, *Recurrence plots for the analysis of complex systems*, Physics Reports **438**, 237, (2007).

[32] Marwan, N., N. Wessel, U. Meyerfeldt, A. Schirdewan, and J. Kurths, *Recurrence plot based measures of complexity and its application to heart rate variability data*, Physical Review E, **66**, 026702, (2002).

[33] Huang, N.E, Z. Seng, S. R. Long, M. C. Wu, H. H. Shih, Q. Zheng, N. Yen, C. C. Thung, H. H. Liu, *The empirical mode decomposition and the Hilbert spectrum for nonlinear and non-stationary time series analysis*, Proc. R. Soc. Lond. A **454**, 903, (1998).

[34] Schwartz, M., W. R. Bennett, and S. Stein, *Communication systems and techniques*, New York: McGraw-Hill, (1966).

[35] Kaplan, D. T., and L. Glass, *Direct test for determinism in a time series*, Physical Review Letters, **68**, 427, (1992).

[36] Theodoridis, S., and K. Koutroumbas, *Pattern recognition*, (2nd edn.), ELSEVIER Academic Press, (2003).

[37] Rypdal, K. and S. Ratynskaia, *Onset of turbulence and profile resilience in the Helimak configuration*, Physical Review Letters **94**, 225002 (2005).

[38] Müller, S. H., A. Fasoli, B. Labit, M. McGrath, M. Podestá, and F. M. Poli, *Effects of a vertical magnetic field on particle confinement in a magnetized plasma torus*, Physical Review Letters, **93**, 16, (2004).

[39] Ukhorskiy, A. Y., M. I. Sitnov, A. S. Sharma, K. Papadopoulos, *Global and multiscale features in a description of the Solar wind-magetopshere coupling*, Annales Geophysicae **21**, 1913, (2003).

[40] Rypdal, K., and S. Ratynskaia, *Statistics of low-frequency plasma fluctuations in a simple magnetized torus*, Physics of Plasmas **10**, 2686 (2003).

[41] Abarbanel, H., *Analysis of observed chaotic data*, Springer, New York, (1996).

[42] Dämming, M., and F. Mitschke, *Estimation of Lyapunov exponents from time series: the stochastic case*, Physics Letters A **178**, 385, (1993).

[43] Theiler, J., *Spurious dimension from correlation algorithms applied to limited time series data*, Physical Review A **34**, 2427, (1986).

[44] Prichard, D., and P. Price, *Spurious dimension estimates from time series of geomagnetic indices*, Geophysical Research Letters **19**, 1623 (1992).

[45] Feldstein, Y. I., V. A. Popov, J. A. Cumnock, A. Prigancova, L. G. Bloomberg, J. U. Kozyra, B. T. Tsurutanj, L. I. Gromova, and A. E. Levitin, *Auroral electrojets and boundaries of plasma domains in the magnetosphere during magnetically disturbed intervals*, Annales Geophysicae, **24**, 2243, (2006).

[46] Akasofu, S. I., *The development of the auroral substorm*, Planetary and Space Science, **12**, 273, (1964).

[47] Akasofu, S. I., *Energy coupling between the solar wind and the magnetosphere*, Space Science Reviews, **28**, 121, (1981).

[48] Angelopoulos, V, T. Mukai, and S. Kokobun, *Evidence for intermittency in Earth's plasma sheet and implications for self-organized criticality*, Physics of Plasmas, **6**, 4161, (1999).

[49] Watkins, N. W., *Scaling in the space climatology of the auroral indices: is SOC the only possible description*, Nonlinear Processes in Geophysics **9**, 389, (2002).

[50] Uritsky, V., A. Klimas, D. Vassiliadis, D. Chua, and G. Parks, *Scale-free statistics of spatio-temporal auroral emissions as depicted by POLAR UVI images: the dynamic magnetosphere is an avalanching system* , Journal of Geophysical Research, **107**, (2002).

[51] Kozelov, B. V., V. M. Uritsky, A. J. Klimas, *Power law probability distributions of multiscale auroral dynamics from ground-based TV observations*, Geophysical Research Letters, **31**, L20804, (2004).

[52] Chapman, S. C., N. W. Watkins, R. O. Dendy, P. Helander, and G. Rowlands, *A simple avalanche model as an analogue for magnetospheric activity*, Geophysical Research Letters, **25**, 2397, (1998).

[53] Consolini, G., and T. Chang, *Magnetic field topology and criticality in geotail dynamics: Relevance to substorm phenomena*, Space Science Review, **95**, 309, (2001).

[54] Sitnov, M. I, A. S. Sharma, and K. Papadopoulos, *Modeling substorm dynamics of the magnetosphere: From self-organization and self-organized criticality to nonequilibrium phase transitions*, Physical Review E, **65**, 016116, (2001).

[55] Klimas, A. J., D. Vassiliadis, D. N. Baker, and D. A. Roberts, *The organized nonlinear dynamics of the magnetosphere*, Journal of Geophysical Research, **101**, 13089, (1996).

[56] Athanasiu, M. A., and G. P. Pavlos, *SVD analysis of the magnetospheric AE index time series and comparison with low-dimensional chaotic dynamics*, Nonlininear Processes in Geophysics, **8**, 95, (2001).

[57] Watkins, N. W., M. P. Freeman, S. C. Chapman, and R. O. Dendy, *Testing the SOC hypothesis for the magnetosphere*, Journal of Atmospheric and Solar- Terrestrial Physics **63**, 1435, (2001).

[58] Deser, C., M. A. Alexander, S-P. Xie, and A. S. Phillips, *Sea surface temperature variability: Patterns and mechanisms*, The annual Review of Marine Sciences **2**, 115-43, (2010).

[59] Franzke, C, *Multi-scale analysis of teleconnection indices: climate noise and nonlinear trend analysis*, Nonlinear Processes in Geophysics, **16**, 65, (2009).

[60] Delworth, T., R. J. Greatbatch, *Multidecadal thermohaline circulation variability driven by atmospheric surface flux forcing*, Journal of Climate **13**, 1481, (2000).

[61] Ghil, M., I. Zaliapin, and S. Thompson, *A dealy differential model of ENSO variability: parametric instability and the distribution of extremes*, Nonlinear Processes in Geophysics, **15**, 417, (2008).

[62] Tziperman, E., L. Stone, M. Cane, and H. Jarosh, *El Niño chaos: Overlapping of resonances between the seasonal cycle and the Pacific ocean-atmosphere oscillator*, Science **264**, 72-74, (1994).

[63] Kaplan, D. T., and L. Glass, *Coarse-grained embedding of time series: random walks, Gaussian random processes, and deterministic chaos*, Physica D, **64**, 431, (1993).

ISBN xxx-xx-xxxx-xxx-x